Available online at www.sciencedirect.com

ScienceDirect

Comput. Methods Appl. Mech. Engrg. 300 (2016) 84–105

Computer methods in applied mechanics and engineering

www.elsevier.com/locate/cma

Perturbation-based stochastic multi-scale computational homogenization method for the determination of the effective properties of composite materials with random properties

X.-Y. Zhou[a], P.D. Gosling[a,*], C.J. Pearce[b], Ł. Kaczmarczyk[b], Z. Ullah[b]

[a] *School of Civil Engineering & Geosciences, Newcastle University, Newcastle, NE1 7RU, UK*
[b] *School of Engineering, University of Glasgow, Glasgow, G12 8QQ, UK*

Received 5 December 2014; received in revised form 18 August 2015; accepted 15 October 2015
Available online 17 November 2015

Abstract

Quantifying uncertainty in the overall elastic properties of composite materials arising from randomness in the material properties and geometry of composites at microscopic level is crucial in the stochastic analysis of composites. In this paper, a stochastic multi-scale finite element method, which couples the multi-scale computational homogenization method with the second-order perturbation technique, is proposed to calculate the statistics of the overall elasticity properties of composite materials in terms of the mean value and standard deviation. The uncertainties associated with the material properties of the constituents are considered. Performance of the proposed method is evaluated by comparing mean values and coefficients of variation for components of the effective elastic tensor against corresponding values calculated using Monte Carlo simulation for three numerical examples. Results demonstrate that the proposed method has sufficient accuracy to capture the variability in effective elastic properties of the composite induced by randomness in the constituent material properties.

Keywords: Composites; Effective elastic properties; Computational multi-scale homogenization; Stochastic finite element method; Perturbation technique

1. Introduction

Given the opportunities they present to design for high-performance, composite materials have found extensive applications in a broad range of engineering fields. At the same time they have stimulated enormous research interest. It is the heterogeneous nature of composite materials at the microstructure level that makes the direct (micro-scale) modelling of the material behaviour impractical at structural or component scales.

An important issue when designing with composite materials is to be able to describe adequately the overall material properties on the basis of material parameters of the constituents, such that the structural or mechanical

* Corresponding author.
E-mail addresses: xiaoyi.zhou@newcastle.ac.uk (X.-Y. Zhou), p.d.gosling@newcastle.ac.uk (P.D. Gosling), chris.pearce@glasgow.ac.uk (C.J. Pearce), lukasz.kaczmarczyk@glasgow.ac.uk (Ł. Kaczmarczyk), zahur.ullah@glasgow.ac.uk (Z. Ullah).

http://dx.doi.org/10.1016/j.cma.2015.10.020
0045-7825/

safety of the system can be demonstrated. This requirement demands some knowledge or consideration of variability or uncertainty. The composite material may exhibit uncertainties in the constituent material properties, geometries at various scales, fibre volume fraction, and matrix porosity, for example. The uncertainty in these parameters leads to variability of the mechanical behaviour for the composite which may be reflected in its structural performance.

Conventionally, deterministic composite material properties may be obtained by means of analytical or semi-analytical homogenization techniques [1–3], for example. Computational homogenization, also referred to as FE^2, is a nested finite element method that, in recent years, has proven to be very effective [4]. The work presented in this paper is based on the computational homogenization method proposed in [5] coupled with the influence and quantification of uncertainty in the properties of composite materials.

Several studies have revealed that a serious overestimation or underestimation of the structural reliability may be made when the stochastic nature of the material properties is not taken into account [6–13]. Thus, it is desirable for an accurate prediction of the uncertainty in the mechanical properties of composite materials arising from randomness of the material properties of constituents. The stochastic finite element method is an efficient technique for uncertainty quantification [14]. In recent years, several studies of uncertainty analysis using the multi-scale finite element method have been reported, where stochastic analyses have been undertaken using Monte-Carlo simulation with different finite element schemes [15–20]. Such an approach can become expensive in terms of computational time, especially for large numbers of variables, which is common for composites. In considering the variation of material properties as a function of uncertainty, the perturbation-based stochastic finite element approach [21,22] has been shown to be effective [12,11,13,23]. In [24–28], the spectral stochastic method was used to implement the numerical approximation of a stochastic homogenization problem. Although increasing interest has been found in the stochastic homogenization method for heterogeneous materials, little attention has been paid to the recently developed computational homogenization methods.

In order to obtain better predictive modelling of material behaviour, and to deal with variability in the material properties of each component of the composite, a stochastic multi-scale method is developed by integrating the perturbation based stochastic finite element with a multi-scale computational homogenization method for the probabilistic prediction of the mechanical properties of a composite material. The computational homogenization framework presented by [5,29] is used as the basis for developing the stochastic homogenization method. The first step of the method relies on the construction of a probabilistic model of the microstructure. We then use the perturbation technique to approximate the stochastic function via a Taylor series expansion.

The paper is organized as follows. In the next section, the micro-to-macro transition for the multi-scale modelling method is briefly reviewed. In Section 3, a new perturbation-based stochastic multi-scale finite element method (PSMFE) for probabilistic analysis of the mechanical properties of a composite is described. Finite element implementation of the proposed method is described in Section 4. Formulae to calculate the mean value and covariance of the effective elastic properties are given in Section 5. The accuracy and the computational efficiency of the developed formulation are demonstrated through three examples in Section 6. Conclusions drawn from the present study are provided in the last section.

2. Multi-scale computational homogenization theory

The computational homogenization method can generally be illustrated as in Fig. 1, which is based on three important assumptions: (i) the characteristic size of the microstructure is small compared to that of the macrostructure; (ii) the volume average of the microscopic strain/stress must be equal to the macroscopic strain/stress; and (iii) the volume average of the microscopic stress power must be equal to the macroscopic stress power. The homogenization can be realized in three steps: (1) apply a given macrostrain to the representative volume element (RVE) using appropriate boundary conditions; (2) solve the RVE boundary value problem; (3) calculate the effective macroscopic stress using the volume averaging theorem. Details of the computational homogenization method for heterogeneous materials adopted in this work can be found in [5,30,31]. In what follows we briefly present this computational scheme, following the notation adopted by [5].

Let $\mathbf{x}$ be the position of a point in the macro-continuum. Its microstructure is represented by a unit cell, whose domain is denoted Ω_μ, and is referred to as the RVE. The domain of the RVE is assumed to consist in general of a solid part, Ω_μ^s, and a void part, Ω_μ^v: $\Omega_\mu = \Omega_\mu^s \cup \Omega_\mu^v$. For composites, the solid part, Ω_μ^s, consists of matrix, Ω_μ^m, and fibres, Ω_μ^f: $\Omega_\mu^s = \Omega_\mu^m \cup \Omega_\mu^f = \left(\cup_{i=1}^{k} \Omega_\mu^i\right)^m \cup \left(\cup_{j=1}^{l} \Omega_\mu^j\right)^f$.

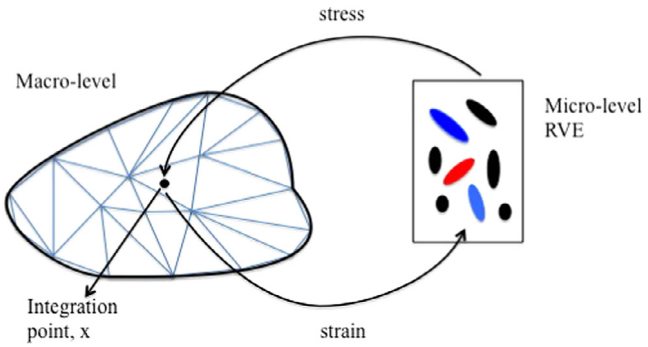

Fig. 1. Illustration of computational homogenization scheme.

2.1. Macro-to-micro transition

Under a given macroscopic strain $\boldsymbol{\varepsilon}$, the displacement field within the RVE associated with a point $\mathbf{x}$ in the macro-continuum is defined as

$$\mathbf{u}_\mu(\mathbf{y}, t) = \boldsymbol{\varepsilon}(\mathbf{x}, t)\mathbf{y} + \tilde{\mathbf{u}}_\mu(\mathbf{y}, t) \tag{1}$$

which is a sum of a linear displacement, $\boldsymbol{\varepsilon}\mathbf{y}$, and a displacement fluctuation, $\tilde{\mathbf{u}}_\mu$. In the following, $\mathbf{y}$ denotes the local coordinate of the RVE. The microscopic terms are described with subscript μ.

Taking the spatial derivative of Eq. (1), the microscopic strain field within the RVE can thus be written as the sum,

$$\boldsymbol{\varepsilon}_\mu(\mathbf{y}, t) = \nabla^s \mathbf{u}_\mu = \boldsymbol{\varepsilon}(\mathbf{x}, t) + \tilde{\boldsymbol{\varepsilon}}_\mu(\mathbf{y}, t) \tag{2}$$

of a homogeneous strain $\boldsymbol{\varepsilon}$, and a strain field,

$$\tilde{\boldsymbol{\varepsilon}}_\mu = \nabla^s \tilde{\mathbf{u}}_\mu \tag{3}$$

that is induced by the displacement fluctuation $\tilde{\mathbf{u}}_\mu$.

Enforcing the assumption relating the microscopic strain and the macroscopic strain, the volume average of the microstrain yields

$$\boldsymbol{\varepsilon}(\mathbf{x}, t) \equiv \frac{1}{V_\mu}\int_\Omega \boldsymbol{\varepsilon}_\mu(\mathbf{y}, t)dV = \boldsymbol{\varepsilon}(\mathbf{x}, t) + \frac{1}{V_\mu}\int_\Omega \tilde{\boldsymbol{\varepsilon}}_\mu(\mathbf{y}, t)dV \tag{4}$$

where $V_\mu = \|\Omega_\mu\|$ is the volume of the RVE. The identity Eq. (4) implies that the estimate of the microstrain $\tilde{\boldsymbol{\varepsilon}}_\mu$, or the displacement fluctuation $\tilde{\mathbf{u}}_\mu$, needs to satisfy the constraint

$$\int_\Omega \tilde{\boldsymbol{\varepsilon}}_\mu(\mathbf{y}, t)dV = \int_\Omega \nabla^s \tilde{\mathbf{u}}_\mu(\mathbf{y}, t)dV = \mathbf{0}. \tag{5}$$

2.2. Micro-to-macro transition

According to the principle of virtual word, the RVE is in equilibrium if, and only if, the variational equation

$$\int_{\Omega_\mu^s} \boldsymbol{\sigma}_\mu(\mathbf{y}, t) : \nabla^s \boldsymbol{\eta} dV - \int_{\partial\Omega_\mu} \mathbf{t}^e \cdot \boldsymbol{\eta} dA = 0 \quad \forall \boldsymbol{\eta} \in \mathcal{V}_\mu \tag{6}$$

holds at each time t, where $\mathcal{V}_\mu$ is an appropriate space of virtual displacements of the RVE, and $\mathbf{t}^e$ denotes tractions on the boundary of the RVE.

The second assumption, also known as the Hill–Mandel principle, requires that the equation

$$\boldsymbol{\sigma} : \dot{\boldsymbol{\varepsilon}} = \frac{1}{V_\mu}\int_{\Omega_\mu^s} \boldsymbol{\sigma}_\mu : \dot{\boldsymbol{\varepsilon}}_\mu dV \tag{7}$$

must hold for any kinematically admissible microscopic strain rate field, $\dot{\boldsymbol{\varepsilon}}_\mu$.

Accordingly, the macroscopic stress tensor, $\boldsymbol{\sigma}$, is taken as the volume average of the microscopic stress field, $\boldsymbol{\sigma}_\mu$, over the RVE:

$$\boldsymbol{\sigma}(\mathbf{x}, t) \equiv \frac{1}{V_\mu} \int_{\Omega_\mu^s} \boldsymbol{\sigma}_\mu(\mathbf{y}, t) dV. \tag{8}$$

By combining Eq. (6) with Eq. (7) and taking Eqs. (2) and (8) into account, we can establish that Eq. (7) is equivalent to the following variational equation:

$$\int_{\partial\Omega_\mu} \mathbf{t}^e \cdot \boldsymbol{\eta} dA = 0 \quad \forall \boldsymbol{\eta} \in \mathcal{V}_\mu \tag{9}$$

in terms of the RVE boundary traction, $\mathbf{t}^e$.

2.3. The RVE equilibrium problem

As a consequence of Eq. (9), the variational equilibrium statement Eq. (6) for the RVE is reduced to

$$G(\boldsymbol{\varepsilon}, \tilde{\mathbf{u}}_\mu, \boldsymbol{\eta}) \equiv \int_{\Omega_\mu^s} \boldsymbol{\sigma}_\mu(\mathbf{y}, t) : \nabla^s \boldsymbol{\eta} dV = 0 \quad \forall \boldsymbol{\eta} \in \mathcal{V}_\mu \tag{10}$$

when ignoring the traction $\mathbf{t}^v$ on interface between void and solid.

Further, we assume that at any time t the stress at each point $\mathbf{y}$ of the RVE is defined by a generic constitutive function $\mathfrak{F}_y$ of the strain history $\boldsymbol{\varepsilon}_\mu^t(\mathbf{y}) = \boldsymbol{\varepsilon}_\mu(\mathbf{y}, t)$ at the point up to time t:

$$\boldsymbol{\sigma}(\mathbf{y}, t) = \mathfrak{F}_y \left(\boldsymbol{\varepsilon}_\mu^t(\mathbf{y}) \right). \tag{11}$$

This constitutive assumption, together with the equilibrium equation (10), leads to the definition of the RVE equilibrium problem which consists in finding, for a given macroscopic strain $\boldsymbol{\varepsilon}$, a displacement fluctuation function $\tilde{\mathbf{u}}_\mu \in \mathcal{V}_\mu$ such that

$$\int_{\Omega_\mu^s} \mathfrak{F}_y \left\{ \left[\boldsymbol{\varepsilon} + \nabla^s \tilde{\mathbf{u}}_\mu(\mathbf{y}) \right]^t \right\} : \nabla^s \boldsymbol{\eta} dV = 0 \quad \forall \boldsymbol{\eta} \in \mathcal{V}_\mu. \tag{12}$$

2.4. Boundary condition problems

To solve Eq. (12) under the constraints of Eqs. (5) and (9), three classes of RVE kinematic constraints are commonly employed within the multi-scale framework:

- Linear displacements on the RVE boundary. This constraint assumes that the displacement field on the boundary, $\partial\Omega$, of the RVE satisfies

$$\mathbf{u}_\mu(\mathbf{y}, t) = \boldsymbol{\varepsilon}(\mathbf{x}, t)\mathbf{y} \quad \forall \mathbf{y} \in \partial\Omega, \tag{13}$$

  the displacement fluctuations thus vanish on $\partial\Omega$ with $\tilde{\mathbf{u}}_\mu(\mathbf{y}, t) = \mathbf{0}$.
- Periodic displacement fluctuations and anti-periodic tractions on RVE boundary. In this case, it is assumed that the displacement fluctuation is periodic on the boundary of the RVE, it thus requires

$$\tilde{\mathbf{u}}(\mathbf{y}^+, t) = \tilde{\mathbf{u}}(\mathbf{y}^-, t) \tag{14}$$

  for each pair of boundary points $\{\mathbf{y}^+, \mathbf{y}^-\}$. Together with the constraint Eq. (9), the traction on the boundary should be

$$\mathbf{t}^e(\mathbf{y}^+, t) = -\mathbf{t}^e(\mathbf{y}^-, t) \tag{15}$$

  anti-periodic for corresponding pair of points $\{\mathbf{y}^+, \mathbf{y}^-\}$.

- Constant traction. This type of constraint, which is derived under the assumption of minimum kinematic constraint on the RVE, assumes that the tractions on the boundary of the RVE can be prescribed as

$$\mathbf{t}^e(\mathbf{y},t) = \boldsymbol{\sigma}_\mu(\mathbf{y},t)\mathbf{n} = \boldsymbol{\sigma}(\mathbf{x},t)\mathbf{n}(\mathbf{y}) \quad \forall \mathbf{y} \in \partial\Omega_\mu \tag{16}$$

where $\boldsymbol{\sigma}$ is previously defined macroscopic stress, and $\mathbf{n}$ is the unit normal vector to the solid domain boundary.

3. Stochastic variational formulation of multi-scale homogenization

3.1. Stochastic second-order perturbation of the homogenization equation

In this work, we consider that the constituents of the composite are linear elastic materials, with the extension to non-linear constitutive behaviour the subject of future research. Therefore, we have

$$\boldsymbol{\sigma}_\mu(\mathbf{y},t) = \mathscr{F}\left\{\left[\boldsymbol{\varepsilon} + \nabla^s \tilde{u}_\mu\right]^t\right\} = \mathbb{C}_\mu\left(\boldsymbol{\varepsilon} + \nabla^s \tilde{u}_\mu\right) \tag{17}$$

with $\mathbb{C}_\mu$ denoting the microscale material constitutive law. Under this consideration, the RVE equilibrium problem in Eq. (12) is equivalent to solving the following linear variational equation for the field $\tilde{\mathbf{u}}_\mu \in \mathscr{V}_\mu$ under a given $\boldsymbol{\varepsilon}$,

$$\int_{\Omega_\mu^s} \nabla^s \boldsymbol{\eta} : \mathbb{C}_\mu : \nabla^s \tilde{\mathbf{u}}_\mu dV = -\left[\int_{\Omega_\mu^s} \nabla^s \boldsymbol{\eta} : \mathbb{C}_\mu dV\right] : \boldsymbol{\varepsilon} \quad \forall \boldsymbol{\eta} \in \mathscr{V}_\mu. \tag{18}$$

We now consider variations in constituent material properties and define $\mathbf{b} = \{b_1, b_2, \ldots, b_n\}^T$ as an n-dimensional random vector, that, in the present case, comprises Young's moduli, Poisson's ratios, and shear moduli. In Eq. (18), the constitutive matrix $\mathbb{C}_\mu$, being a function of the material properties, is thus a stochastic function. Furthermore the resulting microscopic displacement fluctuation field $\tilde{\mathbf{u}}_\mu$ is also a stochastic function of the material properties.

According to the perturbation technique [21,22], an arbitrary stochastic function, $F(\mathbf{b})$, of the random vector $\mathbf{b}$ can be approximated via Taylor series expansion:

$$F(\mathbf{b}) = F(\bar{\mathbf{b}}) + \epsilon \sum_{i=1}^{n} \left[D_{b_i} F(\bar{\mathbf{b}})\right] \delta b_i + \epsilon^2 \frac{1}{2} \sum_{i=1}^{n} \sum_{j=1}^{n} \left[H_{b_i b_j} F(\bar{\mathbf{b}})\right] \delta b_i \delta b_j \tag{19}$$

in the case of a second-order approximation, where $\bar{\mathbf{b}}$ is the mean value of the random vector $\mathbf{b}$; $D_{b_i}(\cdot)$ and $H_{b_i b_j}(\cdot)$ denote the first- and second-order partial derivatives of $(\cdot)$, and ϵ is a scalar representing a given small perturbation.

By expanding the stochastic functions $\mathbb{C}_\mu$, $\tilde{\mathbf{u}}_\mu$ and $\nabla^s \tilde{\mathbf{u}}_\mu$ in Eq. (18) to the forms similar to Eq. (19) and substituting into Eq. (18), and equating terms of equal orders of ϵ, we arrive at the following zeroth-, first- and second-order virtual work principles:

- Zeroth-order (ϵ^0 term)

$$\int_{\Omega_\mu^s} \nabla^s \boldsymbol{\eta} : \mathbb{C}_\mu(\bar{\mathbf{b}}) : \nabla^s \tilde{\mathbf{u}}_\mu(\bar{\mathbf{b}}) + \int_{\Omega_\mu^s} \nabla^s \boldsymbol{\eta} : \mathbb{C}_\mu(\bar{\mathbf{b}}) : \boldsymbol{\varepsilon} dV = 0. \tag{20}$$

- First-order (ϵ^1 term)

$$\sum_{p=1}^{n} \left\{ \int_{\Omega_\mu^s} \nabla^s \boldsymbol{\eta} : \left(\mathbb{C}_\mu(\bar{\mathbf{b}}) : \left[D_{b_p} \nabla^s \tilde{\mathbf{u}}_\mu(\bar{\mathbf{b}})\right] + \left[D_{b_p} \mathbb{C}_\mu(\bar{\mathbf{b}})\right] : \nabla^s \tilde{\mathbf{u}}_\mu(\bar{\mathbf{b}})\right) dV \right.$$
$$\left. + \int_{\Omega_\mu^s} \nabla^s \boldsymbol{\eta} : \left[D_{b_p} \mathbb{C}_\mu(\bar{\mathbf{b}})\right] : \boldsymbol{\varepsilon} dV \right\} \delta b_p = 0. \tag{21}$$

- Second-order (ϵ^2 term)

$$\sum_{p=1}^{n} \sum_{q=1}^{n} \left\{ \int_{\Omega_\mu^s} \nabla^s \boldsymbol{\eta} : \left(\mathbb{C}_\mu(\bar{\mathbf{b}}) : \left[H_{b_p b_q} \nabla^s \tilde{\mathbf{u}}_\mu(\bar{\mathbf{b}})\right] + \left[H_{b_p b_q} \mathbb{C}_\mu(\bar{\mathbf{b}})\right] : \nabla^s \tilde{\mathbf{u}}_\mu(\bar{\mathbf{b}}) \right.\right.$$
$$\left.\left. + 2\left[D_{b_p} \mathbb{C}_\mu(\bar{\mathbf{b}})\right] : \left[D_{b_q} \nabla^s \tilde{\mathbf{u}}_\mu(\bar{\mathbf{b}})\right]\right) dV + \int_{\Omega_\mu^s} \nabla^s \boldsymbol{\eta} : \left[H_{b_p b_q} \mathbb{C}_\mu(\bar{\mathbf{b}})\right] : \boldsymbol{\varepsilon} dV \right\} \delta b_p \delta b_q = 0. \tag{22}$$

3.2. Finite element discretization and solution

Using standard notations as follows,

$$\tilde{\mathbf{u}}_\mu = \mathbf{N}\tilde{\mathbf{a}}_\mu, \qquad \nabla^s\tilde{\mathbf{u}}_\mu = \mathbf{B}\tilde{\mathbf{a}}_\mu, \qquad \boldsymbol{\eta} = \mathbf{N}\delta\mathbf{a}, \qquad \nabla^s\boldsymbol{\eta} = \mathbf{B}\delta\mathbf{a} \quad \text{and} \quad \boldsymbol{\varepsilon} = \mathbf{B}\mathbf{a}^*, \tag{23}$$

where $\mathbf{N}$ denotes shape function, $\mathbf{B}$ is the strain–displacement matrix, $\tilde{\mathbf{a}}_\mu$ is nodal displacement fluctuation vector, $\delta\mathbf{a}$ is virtual nodal displacement fluctuation vector, $\mathbf{a}^*$ denotes the given nodal displacement vector. The finite element approximation to the zeroth-, first- and second-order variational principles, respectively is obtained as:

- The zeroth-order

$$\left\{\mathbf{K}\tilde{\mathbf{a}}_\mu + \mathbf{K}\mathbf{a}^*\right\} \cdot \delta\mathbf{a} = \mathbf{0}. \tag{24}$$

- The first-order

$$\left\{\sum_{p=1}^{n}\left\{\mathbf{K}\left[D_{b_p}\tilde{\mathbf{a}}_\mu\right] + \left[D_{b_p}\mathbf{K}\right]\tilde{\mathbf{a}}_\mu + \left[D_{b_p}\mathbf{K}^{\cdot p}\right]\mathbf{a}^*\right\}\delta b_p\right\} \cdot \delta\mathbf{a} = \mathbf{0}. \tag{25}$$

- The second-order

$$\left\{\sum_{p=1}^{n}\sum_{q=1}^{n}\left\{\mathbf{K}\left[H_{b_pb_q}\tilde{\mathbf{a}}_\mu\right] + \left[H_{b_pb_q}\mathbf{K}\right]\tilde{\mathbf{a}}_\mu + 2\left[D_{b_p}\mathbf{K}\right]\left[D_{b_p}\tilde{\mathbf{a}}_\mu\right] + \left[H_{b_pb_q}\mathbf{K}\right]\mathbf{a}^*\right\}\delta b_p\delta b_q\right\} \cdot \delta\mathbf{a} = \mathbf{0} \tag{26}$$

with

$$\begin{aligned} &\mathbf{K} = \int_{\Omega_\mu^s}\mathbf{B}^T\mathbb{C}_\mu\mathbf{B}dV, \qquad \left[D_{b_p}\mathbf{K}\right] = \int_{\Omega_\mu^s}\mathbf{B}^T\left[D_{b_p}\mathbb{C}_\mu\right]\mathbf{B}dV, \quad \text{and} \\ &\left[H_{b_pb_q}\mathbf{K}\right] = \int_{\Omega_\mu^s}\mathbf{B}^T\left[H_{b_pb_q}\mathbb{C}_\mu\right]\mathbf{B}dV \end{aligned} \tag{27}$$

denoted as the stiffness matrix and its first- and second-order partial derivatives, respectively. With the solution $\tilde{\mathbf{a}}_\mu$ and its derivatives $\left[D_{b_p}\tilde{\mathbf{a}}_\mu\right]$ and $\left[H_{b_pb_q}\tilde{\mathbf{a}}_\mu\right]$ at hand, the displacement field $\mathbf{a}$ of the microstructure can be straightforwardly computed. Hence, the stochastic estimates of the other quantities, for instance, stress, can be calculated.

4. Finite element implementation for the specific classes of boundary constraints

As previously mentioned, the solution of displacement fluctuations and their derivatives for Eqs. (24)–(26) need to satisfy the constraints of Eqs. (5) and (9). We now detail the stochastic finite element implementation procedures for the considered three classes of classic boundary conditions in Eqs. (13)–(16). In accord with the discrete formulation of the boundary conditions outlined earlier, the nodal displacements, internal forces and stiffness matrix are partitioned into those on the boundary (denoted by subscript b) and those in the interior (subscript i) of the RVE as:

$$[\mathbf{a}]_{n\times 1} = \begin{Bmatrix}[\mathbf{a}_i]_{n_i\times 1}\\ [\mathbf{a}_b]_{n_b\times 1}\end{Bmatrix} \equiv \begin{Bmatrix}\mathbb{L}_i\mathbf{a}\\ \mathbb{L}_b\mathbf{a}\end{Bmatrix} \tag{28}$$

and

$$[\mathbf{f}]_{n\times 1} = \begin{Bmatrix}[\mathbf{f}_i]_{n_i\times 1}\\ [\mathbf{f}_b]_{n_b\times 1}\end{Bmatrix} \equiv \begin{Bmatrix}\mathbb{L}_i\mathbf{f}\\ \mathbb{L}_b\mathbf{f}\end{Bmatrix} \tag{29}$$

$$[\mathbf{K}]_{n\times n} = \begin{bmatrix}[\mathbf{K}_{ii}]_{n_i\times n_i} & [\mathbf{K}_{ib}]_{n_i\times n_b}\\ [\mathbf{K}_{bi}]_{n_b\times n_i} & [\mathbf{K}_{bb}]_{n_b\times n_b}\end{bmatrix} \equiv \begin{bmatrix}\mathbb{L}_i\mathbf{K}\mathbb{L}_i^T & \mathbb{L}_i\mathbf{K}\mathbb{L}_b^T\\ \mathbb{L}_b\mathbf{K}\mathbb{L}_i^T & \mathbb{L}_b\mathbf{K}\mathbb{L}_b^T\end{bmatrix}. \tag{30}$$

Here $\mathbb{L}_i$ and $\mathbb{L}_b$ are the connectivity matrices that define the contributions of the interior and boundary nodes, respectively. These are Boolean matrices, i.e. they consist of integers 0 and 1.

4.1. Linear displacements on the boundary

For the linear boundary displacements, for instance, the system Eq. (24), reduces to solving

$$\begin{bmatrix}\mathbf{K}_{ii} & \mathbf{K}_{ib}\end{bmatrix}\begin{bmatrix}\mathbf{a}_i^* \\ \mathbf{a}_b^*\end{bmatrix} + \mathbf{K}_{ii}\tilde{\mathbf{a}}_i = \mathbf{0} \tag{31}$$

to obtain the displacement fluctuations of the inner nodes, $\tilde{\mathbf{a}}_i$ with the displacement fluctuations of the boundary in Eq. (13) prescribed as zero. Defining $\mathbf{K}_i$ and $\mathbf{a}^*$ as

$$\mathbf{K}_i = \begin{bmatrix}\mathbf{K}_{ii} & \mathbf{K}_{ib}\end{bmatrix}, \qquad \mathbf{a}^* = \begin{bmatrix}\mathbf{a}_i^* \\ \mathbf{a}_b^*\end{bmatrix}, \tag{32}$$

respectively, Eq. (31) is simplified to

$$\mathbf{K}_i\mathbf{a}^* + \mathbf{K}_{ii}\tilde{\mathbf{a}}_i = \mathbf{0}. \tag{33}$$

Taking into account the Taylor series expansions given by Eq. (19), the stochastic terms $\mathbf{K}_i$, $\mathbf{K}_{ii}$ and $\tilde{\mathbf{a}}_i$ involved in Eq. (33) are expanded into their perturbation forms as

$$\tilde{\mathbf{a}}_i(\mathbf{b}) = \tilde{\mathbf{a}}_i(\bar{\mathbf{b}}) + \epsilon\sum_{r=1}^{n}\left[D_{b_r}\tilde{\mathbf{a}}_i(\bar{\mathbf{b}})\right]\delta b_r + \epsilon^2\frac{1}{2}\sum_{r=1}^{n}\sum_{s=1}^{n}\left[H_{b_rb_s}\tilde{\mathbf{a}}_i(\bar{\mathbf{b}})\right]\delta b_r\delta b_s \tag{34a}$$

$$\mathbf{K}_{ii}(\mathbf{b}) = \mathbf{K}_{ii}(\bar{\mathbf{b}}) + \epsilon\sum_{r=1}^{n}\left[D_{b_r}\mathbf{K}_{ii}(\bar{\mathbf{b}})\right]\delta b_r + \epsilon^2\frac{1}{2}\sum_{r=1}^{n}\sum_{s=1}^{n}\left[H_{b_rb_s}\mathbf{K}_{ii}(\bar{\mathbf{b}})\right]\delta b_r\delta b_s \tag{34b}$$

$$\mathbf{K}_i(\mathbf{b}) = \mathbf{K}_i(\bar{\mathbf{b}}) + \epsilon\sum_{r=1}^{n}\left[D_{b_r}\mathbf{K}_i(\bar{\mathbf{b}})\right]\delta b_r + \epsilon^2\frac{1}{2}\sum_{r=1}^{n}\sum_{s=1}^{n}\left[H_{b_rb_s}\mathbf{K}_i(\bar{\mathbf{b}})\right]\delta b_r\delta b_s. \tag{34c}$$

Substituting them into Eqs. (24)–(26), the reduced zeroth-, first- and second-order finite element equations are obtained as,

$$[\mathbf{K}_i]\left[\mathbf{a}^*\right] + [\mathbf{K}_{ii}]\left[\tilde{\mathbf{a}}_i\right] = \mathbf{0} \tag{35a}$$

$$\sum_{r=1}^{n}\left\{\left[D_{b_r}\mathbf{K}_i\right]\left[\mathbf{a}^*\right] + [\mathbf{K}_{ii}]\left[D_{b_r}\tilde{\mathbf{a}}_i\right] + \left[D_{b_r}\mathbf{K}_{ii}\right]\left[\tilde{\mathbf{a}}_i\right]\right\}\delta b_r = \mathbf{0} \tag{35b}$$

$$\sum_{r=1}^{n}\sum_{s=1}^{n}\left\{\left[H_{b_rb_s}\mathbf{K}_i\right]\left[\mathbf{a}^*\right] + 2\left[D_{b_r}\mathbf{K}_{ii}\right]\left[D_{b_s}\tilde{\mathbf{a}}_i\right] + [\mathbf{K}_{ii}]\left[H_{b_rb_s}\tilde{\mathbf{a}}_i\right] + \left[H_{b_rb_s}\mathbf{K}_{ii}\right]\left[\tilde{\mathbf{a}}_i\right]\right\}\delta b_r\delta b_s = \mathbf{0}. \tag{35c}$$

Computing the above equations successively, the zeroth order displacement fluctuation vector $\left[\tilde{\mathbf{a}}_i(\bar{\mathbf{b}})\right]$ can be derived from Eq. (35a), the first order partial derivative of displacement fluctuation vector $\left[D_{b_r}\tilde{\mathbf{a}}_i(\bar{\mathbf{b}})\right]$ from Eq. (35b), and the second order partial derivative of displacement fluctuation vector $\left[H_{b_rb_s}\tilde{\mathbf{a}}_i(\bar{\mathbf{b}})\right]$ from Eq. (35c).

4.2. Periodic displacements and anti-periodic tractions on the boundary

Under the assumption of periodic boundary displacement fluctuations, nodes on the RVE boundary need to be sub-divided further as

$$\mathbf{a}_b = \begin{bmatrix}\mathbf{a}_p & \mathbf{a}_n & \mathbf{a}_c\end{bmatrix} \tag{36}$$

where the subscripts p, n and c denote positive boundary nodes, negative boundary nodes and corner nodes, respectively. Hence, the node displacements of the mesh are partitioned as

$$[\mathbf{a}]_{n\times 1} = \begin{Bmatrix}[\mathbf{a}_i]_{n_i\times 1} \\ [\mathbf{a}_b]_{n_b\times 1}\end{Bmatrix} = \begin{Bmatrix}[\mathbf{a}_i]_{n_i\times 1} \\ [\mathbf{a}_p]_{n_p\times 1} \\ [\mathbf{a}_n]_{n_n\times 1} \\ [\mathbf{a}_c]_{n_c\times 1}\end{Bmatrix} \equiv \begin{Bmatrix}\mathbb{L}_i\mathbf{a} \\ \mathbb{L}_p\mathbf{a} \\ \mathbb{L}_n\mathbf{a} \\ \mathbb{L}_c\mathbf{a}\end{Bmatrix}. \tag{37}$$

According to Eq. (1), the nodal displacement field is further decomposed into a prescribed part, denoted as $\mathbf{a}^*$, and a fluctuation part, denoted as $\tilde{\mathbf{a}}$, as follows:

$$[\mathbf{a}]_{n\times 1} = \begin{Bmatrix} [\mathbf{a}_i^*]_{n_i\times 1} \\ [\mathbf{a}_p^*]_{n_p\times 1} \\ [\mathbf{a}_n^*]_{n_n\times 1} \\ [\mathbf{a}_c^*]_{n_c\times 1} \end{Bmatrix} + \begin{Bmatrix} [\tilde{\mathbf{a}}_i]_{n_i\times 1} \\ [\tilde{\mathbf{a}}_p]_{n_p\times 1} \\ [\tilde{\mathbf{a}}_n]_{n_n\times 1} \\ [\tilde{\mathbf{a}}_c]_{n_c\times 1} \end{Bmatrix}. \tag{38}$$

With $\tilde{\mathbf{u}}(\mathbf{y}^+) = \tilde{\mathbf{u}}(\mathbf{y}^-)$ defined in Eq. (14), $\tilde{\mathbf{a}}_p = \tilde{\mathbf{a}}_n$ and $\tilde{\mathbf{a}}_c = \mathbf{0}$. Furthermore, the degrees of freedom for the corner nodes are prescribed as zero, $\mathbf{a}_c^* = \mathbf{0}$, to remove rigid body displacements of the RVE. Accordingly, stiffness matrix $\mathbf{K}$ needs to be divided into 9 blocks to coincide with the pattern of $\mathbf{a}$. Hence, Eq. (24) transforms to

$$\left\{ \begin{bmatrix} \mathbf{K}_{ii} & \mathbf{K}_{ip} & \mathbf{K}_{in} \\ \mathbf{K}_{pi} & \mathbf{K}_{pp} & \mathbf{K}_{pn} \\ \mathbf{K}_{ni} & \mathbf{K}_{np} & \mathbf{K}_{nn} \end{bmatrix} \begin{bmatrix} \mathbf{a}_i^* \\ \mathbf{a}_p^* \\ \mathbf{a}_n^* \end{bmatrix} + \begin{bmatrix} \mathbf{K}_{ii} & \mathbf{K}_{ip} & \mathbf{K}_{in} \\ \mathbf{K}_{pi} & \mathbf{K}_{pp} & \mathbf{K}_{pn} \\ \mathbf{K}_{ni} & \mathbf{K}_{np} & \mathbf{K}_{nn} \end{bmatrix} \begin{bmatrix} \tilde{\mathbf{a}}_i \\ \tilde{\mathbf{a}}_p \\ \tilde{\mathbf{a}}_p \end{bmatrix} \right\} \delta\mathbf{a} = \mathbf{0}. \tag{39}$$

Moreover, the second part of boundary condition in Eq. (15) indicates that the sum of the tractions on positive and negative boundaries is zero. By operating appropriate matrix manipulations, Eq. (24) reduces to the solution of the problem

$$\begin{bmatrix} \mathbf{K}_{ii} & \mathbf{K}_{ip} & \mathbf{K}_{in} \\ \mathbf{K}_{pi}+\mathbf{K}_{ni} & \mathbf{K}_{pp}+\mathbf{K}_{np} & \mathbf{K}_{pn}+\mathbf{K}_{nn} \end{bmatrix} \begin{bmatrix} \mathbf{a}_i^* \\ \mathbf{a}_p^* \\ \mathbf{a}_n^* \end{bmatrix} + \begin{bmatrix} \mathbf{K}_{ii} & \mathbf{K}_{ip}+\mathbf{K}_{in} \\ \mathbf{K}_{pi}+\mathbf{K}_{ni} & \mathbf{K}_{pp}+\mathbf{K}_{np}+\mathbf{K}_{pn}+\mathbf{K}_{nn} \end{bmatrix} \begin{bmatrix} \tilde{\mathbf{a}}_i \\ \tilde{\mathbf{a}}_p \end{bmatrix} = \mathbf{0} \tag{40}$$

for $\tilde{\mathbf{a}}_i$ and $\tilde{\mathbf{a}}_p$ or $\tilde{\mathbf{a}}_n$. For convenience, $\mathbf{a}^*$, $\hat{\mathbf{u}}$, $\mathbf{K}^*$ and $\tilde{\mathbf{K}}$ are defined as,

$$\mathbf{a}^* = \begin{bmatrix} \mathbf{a}_i^* \\ \mathbf{a}_p^* \\ \mathbf{a}_n^* \end{bmatrix}, \qquad \hat{\mathbf{a}} = \begin{Bmatrix} \tilde{\mathbf{a}}_i \\ \tilde{\mathbf{a}}_p \end{Bmatrix} \tag{41}$$

$$\mathbf{K}^* = \begin{bmatrix} \mathbf{K}_{ii} & \mathbf{K}_{ip} & \mathbf{K}_{in} \\ \mathbf{K}_{pi}+\mathbf{K}_{ni} & \mathbf{K}_{pp}+\mathbf{K}_{np} & \mathbf{K}_{pn}+\mathbf{K}_{nn} \end{bmatrix}, \tag{42}$$

$$\tilde{\mathbf{K}} = \begin{bmatrix} \mathbf{K}_{ii} & \mathbf{K}_{ip}+\mathbf{K}_{in} \\ \mathbf{K}_{pi}+\mathbf{K}_{ni} & \mathbf{K}_{pp}+\mathbf{K}_{pn}+\mathbf{K}_{np}+\mathbf{K}_{nn} \end{bmatrix}, \tag{43}$$

respectively. Thus, the Eq. (40) can be re-written in a compact form as

$$\mathbf{K}^*(\mathbf{b})\mathbf{a}^*(\mathbf{b}) + \tilde{\mathbf{K}}(\mathbf{b})\hat{\mathbf{a}}(\mathbf{b}) = \mathbf{0}. \tag{44}$$

Expanding the stochastic terms $\hat{\mathbf{a}}$, $\mathbf{K}^*$ and $\tilde{\mathbf{K}}$ into their perturbation forms as

$$\hat{\mathbf{a}}(\mathbf{b}) = \hat{\mathbf{a}}\left(\bar{\mathbf{b}}\right) + \epsilon \sum_{r=1}^{n} \left[D_{b_r}\hat{\mathbf{a}}\left(\bar{\mathbf{b}}\right)\right] \delta b_r + \epsilon^2 \frac{1}{2} \sum_{r=1}^{n}\sum_{s=1}^{n} \left[H_{b_r b_s}\hat{\mathbf{a}}\left(\bar{\mathbf{b}}\right)\right] \delta b_r \delta b_s \tag{45a}$$

$$\mathbf{K}^*(\mathbf{b}) = \mathbf{K}^*\left(\bar{\mathbf{b}}\right) + \epsilon \sum_{r=1}^{n} \left[D_{b_r}\mathbf{K}^*\left(\bar{\mathbf{b}}\right)\right] \delta b_r + \epsilon^2 \frac{1}{2} \sum_{r=1}^{n}\sum_{s=1}^{n} \left[H_{b_r b_s}\mathbf{K}^*\left(\bar{\mathbf{b}}\right)\right] \delta b_r \delta b_s \tag{45b}$$

$$\tilde{\mathbf{K}}(\mathbf{b}) = \tilde{\mathbf{K}}\left(\bar{\mathbf{b}}\right) + \epsilon \sum_{r=1}^{n} \left[D_{b_r}\tilde{\mathbf{K}}\left(\bar{\mathbf{b}}\right)\right] \delta b_r + \epsilon^2 \frac{1}{2} \sum_{r=1}^{n}\sum_{s=1}^{n} \left[H_{b_r b_s}\tilde{\mathbf{K}}\left(\bar{\mathbf{b}}\right)\right] \delta b_r \delta b_s, \tag{45c}$$

and substituting them into Eqs. (24)–(26), the reduced zeroth-, first- and second-order finite element equations are obtained as,

$$\left[\mathbf{K}^*\right]\left[\mathbf{a}^*\right] + \left[\tilde{\mathbf{K}}\right]\left[\hat{\mathbf{a}}\right] = \mathbf{0} \tag{46a}$$

$$\sum_{r=1}^{n}\left\{\left[D_{b_r}\mathbf{K}^*\right]\left[\mathbf{a}^*\right] + \left[\tilde{\mathbf{K}}\right]\left[D_{b_r}\hat{\mathbf{a}}\right] + \left[D_{b_r}\tilde{\mathbf{K}}\right]\left[\hat{\mathbf{a}}\right]\right\}\delta b_r = \mathbf{0} \tag{46b}$$

$$\sum_{r=1}^{n}\sum_{s=1}^{n}\left\{\left[H_{b_r b_s}\mathbf{K}^*\right]\left[\mathbf{a}^*\right] + \left[\tilde{\mathbf{K}}\right]\left[H_{b_r b_s}\hat{\mathbf{a}}\right] + 2\left[D_{b_r}\tilde{\mathbf{K}}\right]\left[D_{b_s}\hat{\mathbf{a}}\right] + \left[H_{b_r b_s}\tilde{\mathbf{K}}\right]\left[\hat{\mathbf{a}}\right]\right\}\delta b_r \delta b_s = \mathbf{0}. \tag{46c}$$

As in the case of linear displacement boundary conditions, computing the above equations successively, the zeroth order displacement fluctuation vector $\hat{\mathbf{a}}(\bar{\mathbf{b}})$ can be derived from Eq. (46a), the first order partial derivative of displacement fluctuation vector $\left[D_{b_r}\hat{\mathbf{a}}(\bar{\mathbf{b}})\right]$ from Eq. (46b), and the second order partial derivative of displacement fluctuation vector $\left[H_{b_r b_s}\hat{\mathbf{a}}(\bar{\mathbf{b}})\right]$ from Eq. (46c).

4.3. Constant tractions on the boundary

For the constant boundary traction model, the RVE geometry must comply with the constraints defined in the previous section, as in,

$$\mathbf{C}\mathbf{a}_b = \mathbf{0} \tag{47}$$

where $\mathbf{C}$ is the constraint matrix defined in [5]. The nodes of the boundary are partitioned as

$$[\mathbf{a}_b] = \begin{pmatrix} [\mathbf{a}_f]_{n_f\times 1} \\ [\mathbf{a}_d]_{n_d\times 1} \\ [\mathbf{a}_p]_{n_p\times 1} \end{pmatrix} \tag{48}$$

where the subscripts f, d and p stand, respectively, for free, dependent and prescribed degrees of freedom on the boundary of the discrete RVE as defined in [5]. Accordingly, the global constraint matrix is partitioned as

$$\mathbf{C} = \begin{bmatrix}\mathbf{C}_f & \mathbf{C}_d & \mathbf{C}_p\end{bmatrix}. \tag{49}$$

Hence, the displacements of the RVE can be partitioned in the form,

$$\left[\mathbf{a}_{n\times 1}\right] = \begin{pmatrix} [\mathbf{a}_i]_{n_i\times 1} \\ [\mathbf{a}_f]_{n_f\times 1} \\ [\mathbf{a}_d]_{n_d\times 1} \\ [\mathbf{a}_p]_{n_p\times 1} \end{pmatrix} \equiv \begin{pmatrix} \mathbb{L}_i\mathbf{a} \\ \mathbb{L}_f\mathbf{a} \\ \mathbb{L}_d\mathbf{a} \\ \mathbb{L}_p\mathbf{a} \end{pmatrix}. \tag{50}$$

Prescribed degrees of freedom are set as zero to remove rigid body displacements of the RVE. Therefore, the relation between free and dependent degrees of freedom can be established as

$$\mathbf{a}_d = \mathbf{R}\mathbf{a}_f \tag{51}$$

where

$$\mathbf{R} \equiv -\mathbf{C}_d^{-1}\mathbf{C}_f. \tag{52}$$

Furthermore, the displacements are decomposed into two parts as indicated in Eq. (1), and stiffness matrix $\mathbf{K}$ is partitioned to be consistent with $\mathbf{a}$. Accordingly, Eq. (24) transforms to

$$\left\{\begin{bmatrix}\mathbf{K}_{ii} & \mathbf{K}_{if} & \mathbf{K}_{id} \\ \mathbf{K}_{fi} & \mathbf{K}_{ff} & \mathbf{K}_{fd} \\ \mathbf{K}_{di} & \mathbf{K}_{df} & \mathbf{K}_{dd}\end{bmatrix}\begin{bmatrix}\mathbf{a}_i^* \\ \mathbf{a}_f^* \\ \mathbf{a}_d^*\end{bmatrix} + \begin{bmatrix}\mathbf{K}_{ii} & \mathbf{K}_{if} & \mathbf{K}_{id} \\ \mathbf{K}_{fi} & \mathbf{K}_{ff} & \mathbf{K}_{fd} \\ \mathbf{K}_{di} & \mathbf{K}_{df} & \mathbf{K}_{dd}\end{bmatrix}\begin{bmatrix}\tilde{\mathbf{a}}_i \\ \tilde{\mathbf{a}}_f \\ \tilde{\mathbf{a}}_d\end{bmatrix}\right\}\delta\mathbf{a} = \mathbf{0}. \tag{53}$$

Due to the relationship between $\boldsymbol{a}_f$ and $\boldsymbol{a}_d$ in Eq. (51), Eq. (53) can be reduced to the following form after appropriate matrix manipulations

$$\begin{bmatrix} \mathbf{K}_{ii} & \mathbf{K}_{if} & \mathbf{K}_{id} \\ \mathbf{K}_{fi}+\mathbf{R}^T\mathbf{K}_{di} & \mathbf{K}_{ff}+\mathbf{R}^T\mathbf{K}_{df} & \mathbf{K}_{fd}+\mathbf{R}^T\mathbf{K}_{dd} \end{bmatrix} \begin{bmatrix} \mathbf{a}_i^* \\ \mathbf{a}_f^* \\ \mathbf{a}_d^* \end{bmatrix} + \begin{bmatrix} \mathbf{K}_{ii} & \mathbf{K}_{if}+\mathbf{K}_{id}\mathbf{R} \\ \mathbf{K}_{fi}+\mathbf{R}^T\mathbf{K}_{di} & \mathbf{K}_{ff}+\mathbf{R}^T\mathbf{K}_{df}+\mathbf{K}_{fd}\mathbf{R}+\mathbf{R}^T\mathbf{K}_{dd}\mathbf{R} \end{bmatrix} \begin{bmatrix} \tilde{\mathbf{a}}_i \\ \tilde{\mathbf{a}}_f \end{bmatrix} = \mathbf{0} \tag{54}$$

with $\tilde{\mathbf{a}}_i$ and $\tilde{\mathbf{a}}_f$ or $\tilde{\mathbf{a}}_d$ the unknowns. Denoting $\mathbf{a}^*$, $\hat{\mathbf{a}}$, $\mathbf{K}^*$ and $\tilde{\mathbf{K}}$ as

$$\mathbf{a}^* = \begin{bmatrix} \mathbf{a}_i^* \\ \mathbf{a}_f^* \\ \mathbf{a}_d^* \end{bmatrix}, \qquad \hat{\mathbf{a}} = \begin{pmatrix} \tilde{\mathbf{a}}_i \\ \tilde{\mathbf{a}}_f \end{pmatrix} \tag{55}$$

$$\mathbf{K}^* = \begin{bmatrix} \mathbf{K}_{ii} & \mathbf{K}_{if} & \mathbf{K}_{id} \\ \mathbf{K}_{fi}+\mathbf{R}^T\mathbf{K}_{di} & \mathbf{K}_{ff}+\mathbf{R}^T\mathbf{K}_{df} & \mathbf{K}_{fd}+\mathbf{R}^T\mathbf{K}_{dd} \end{bmatrix} \tag{56}$$

$$\tilde{\mathbf{K}} = \begin{bmatrix} \mathbf{K}_{ii} & \mathbf{K}_{if}+\mathbf{K}_{id}\mathbf{R} \\ \mathbf{K}_{fi}+\mathbf{R}^T\mathbf{K}_{di} & \mathbf{K}_{ff}+\mathbf{K}_{fd}\mathbf{R}+\mathbf{R}^T\mathbf{K}_{df}+\mathbf{R}^T\mathbf{K}_{dd}\mathbf{R} \end{bmatrix}, \tag{57}$$

respectively, a compact form of Eq. (54) is obtained as,

$$\left[\mathbf{K}^*(\mathbf{b})\right]\left[\mathbf{a}^*(\mathbf{b})\right] + \left[\tilde{\mathbf{K}}(\mathbf{b})\right]\left[\hat{\mathbf{a}}(\mathbf{b})\right] = \mathbf{0}. \tag{58}$$

As before, expanding the stochastic terms $\mathbf{K}^*$, $\tilde{\mathbf{K}}$ and $\hat{\mathbf{a}}$ into their perturbation forms as

$$\hat{\mathbf{a}}(\mathbf{b}) = \hat{\mathbf{a}}\left(\bar{\mathbf{b}}\right) + \epsilon \sum_{r=1}^{n} \left[D_{b_r}\hat{\mathbf{a}}\left(\bar{\mathbf{b}}\right)\right]\delta b_r + \epsilon^2 \frac{1}{2}\sum_{r=1}^{n}\sum_{s=1}^{n}\left[H_{b_r b_s}\hat{\mathbf{a}}\left(\bar{\mathbf{b}}\right)\right]\delta b_r \delta b_s \tag{59a}$$

$$\mathbf{K}^*(\mathbf{b}) = \mathbf{K}^*\left(\bar{\mathbf{b}}\right) + \epsilon \sum_{r=1}^{n} \left[D_{b_r}\mathbf{K}^*\left(\bar{\mathbf{b}}\right)\right]\delta b_r + \epsilon^2 \frac{1}{2}\sum_{r=1}^{n}\sum_{s=1}^{n}\left[H_{b_r b_s}\mathbf{K}^*\left(\bar{\mathbf{b}}\right)\right]\delta b_r \delta b_s \tag{59b}$$

$$\tilde{\mathbf{K}}(\mathbf{b}) = \tilde{\mathbf{K}}\left(\bar{\mathbf{b}}\right) + \epsilon \sum_{r=1}^{n} \left[D_{b_r}\tilde{\mathbf{K}}\left(\bar{\mathbf{b}}\right)\right]\delta b_r + \epsilon^2 \frac{1}{2}\sum_{r=1}^{n}\sum_{s=1}^{n}\left[H_{b_r b_s}\tilde{\mathbf{K}}\left(\bar{\mathbf{b}}\right)\right]\delta b_r \delta b_s, \tag{59c}$$

and substituting them into Eqs. (24)–(26), the reduced zeroth-, first- and second-order finite element equations are obtained as,

$$\left[\mathbf{K}^*\right]\left[\mathbf{a}^*\right] + \left[\tilde{\mathbf{K}}\right]\left[\hat{\mathbf{a}}\right] = \mathbf{0} \tag{60a}$$

$$\sum_{r=1}^{n}\left\{\left[D_{b_r}\mathbf{K}^*\right]\left[\mathbf{a}^*\right] + \left[\tilde{\mathbf{K}}\right]\left[D_{b_r}\hat{\mathbf{a}}\right] + \left[D_{b_r}\tilde{\mathbf{K}}\right]\left[\hat{\mathbf{a}}\right]\right\}\delta b_r = \mathbf{0} \tag{60b}$$

$$\sum_{r=1}^{n}\sum_{s=1}^{n}\left\{\left[H_{b_r b_s}\mathbf{K}^*\right]\left[\mathbf{a}^*\right] + \left[H_{b_r b_s}\tilde{\mathbf{K}}\right]\left[\hat{\mathbf{a}}\right] + \left[\tilde{\mathbf{K}}\right]\left[H_{b_r b_s}\hat{\mathbf{a}}\right] + 2\left[D_{b_r}\tilde{\mathbf{K}}\right]\left[D_{b_s}\hat{\mathbf{a}}\right]\right\}\delta b_r \delta b_s = \mathbf{0}. \tag{60c}$$

Using the same approach for the preceding boundary condition types, the zeroth order displacement fluctuation vector $\hat{\mathbf{a}}(\bar{\mathbf{b}})$ can be derived from Eq. (60a), the first order partial derivative of displacement fluctuation vector $\left[D_{b_r}\hat{\mathbf{a}}(\bar{\mathbf{b}})\right]$ from Eq. (60b), and the second order partial derivative of displacement fluctuation vector $\left[H_{b_r b_s}\hat{\mathbf{a}}(\bar{\mathbf{b}})\right]$ from Eq. (60c) can be successively computed.

5. Statistics of effective elasticity tensor

The objective of a homogenization procedure is to determine the effective elasticity tensor. According to its definition, the effective elastic moduli can be calculated in the following way [31,29]

$$\mathbb{C} = \frac{\boldsymbol{\sigma}}{\boldsymbol{\varepsilon}} = \frac{1}{V}\mathbb{D}_b\frac{\mathbf{f}_b}{\boldsymbol{\varepsilon}} \tag{61}$$

where $\mathbb{D}_b$ is the boundary coordinate matrix defined by

$$\mathbb{D}_b \equiv \left[\mathbb{D}_1^b \cdots \mathbb{D}_i^b \cdots \mathbb{D}_{n_b}^b\right] \tag{62}$$

with $\mathbb{D}_i^b$ as the coordinate matrix at node i of the microstructure defined in [31]. $\mathbf{f}_b$ is the nodal force vector for nodes on the boundary, the components of which can be calculated by

$$\mathbf{f}_b = [\mathbf{K}_{bi} \quad \mathbf{K}_{bb}]\left[\begin{Bmatrix}\mathbf{u}_i^* \\ \mathbf{u}_b^*\end{Bmatrix} + \begin{Bmatrix}\tilde{\mathbf{u}}_i \\ \tilde{\mathbf{u}}_b\end{Bmatrix}\right] = [\mathbf{K}_b]\left[\mathbf{u}^*\right] + [\mathbf{K}_b]\left[\tilde{\mathbf{u}}\right], \quad \text{with} \quad [\mathbf{K}_b] = [\mathbf{K}_{bi} \quad \mathbf{K}_{bb}]. \tag{63}$$

5.1. Stochastic expression of overall tangent moduli

Clearly, the effective elastic tensor, $\mathbb{C}$, is a stochastic function with respect to the material properties. It can be approximated by the perturbation technique using Taylor series expansion, as,

$$[\mathbb{C}(\mathbf{b})] = \left[\mathbb{C}(\bar{\mathbf{b}})\right] + \epsilon \sum_r^n \left[D_{b_r}\mathbb{C}(\bar{\mathbf{b}})\right]\delta b_r + \epsilon^2 \frac{1}{2}\sum_r^n \sum_s^n \left[H_{b_r b_s}\mathbb{C}(\bar{\mathbf{b}})\right]\delta b_r \delta b_s \tag{64}$$

where the first- and second-order partial derivative terms $\left[D_{b_r}\mathbb{C}(\bar{\mathbf{b}})\right]$ and $\left[H_{b_r b_s}\mathbb{C}(\bar{\mathbf{b}})\right]$ can be calculated by substituting

$$\begin{aligned}\mathbf{f}_b(\mathbf{b}) = &\left\{[\mathbf{K}_b]\left[\mathbf{u}^*\right] + [\mathbf{K}_b]\left[\tilde{\mathbf{u}}\right]\right\} + \epsilon \sum_{r=1}^n \left\{[\mathbf{K}_b]\left[D_{b_r}\tilde{\mathbf{u}}\right] + \left[D_{b_r}\mathbf{K}_b\right]\left[\tilde{\mathbf{u}}\right] + \left[D_{b_r}\mathbf{K}_b\right]\left[\mathbf{u}^*\right]\right\}\delta b_r \\ &+ \epsilon^2 \frac{1}{2}\sum_{r=1}^n \sum_{s=1}^n \left\{[\mathbf{K}_b]\left[H_{b_r b_s}\tilde{\mathbf{u}}\right] + 2\left[D_{b_r}\mathbf{K}_b\right]\left[D_{b_s}\tilde{\mathbf{u}}\right] + \left[H_{b_r b_s}\mathbf{K}_b\right]\left[\tilde{\mathbf{u}}\right] + \left[H_{b_r b_s}\mathbf{K}_b\right]\left[\mathbf{u}_i^*\right]\right\}\delta b_r \delta b_s\end{aligned} \tag{65}$$

into Eq. (61) with derivatives of $\mathbf{K}$ and previously calculated $\tilde{\mathbf{u}}$ from (35), (46) or (60) for the three considered classes of boundary constraints.

5.2. Mean and covariance

The expected value

$$E\left[\mathbb{C}(\mathbf{b})\right] = \int_{-\infty}^{+\infty} \left\{\left[\mathbb{C}(\bar{\mathbf{b}})\right] + \epsilon \sum_r \left[D_{b_r}\mathbb{C}(\bar{\mathbf{b}})\right]\delta b_r + \epsilon^2 \frac{1}{2}\sum_r \sum_s \left[H_{b_r b_s}\mathbb{C}(\bar{\mathbf{b}})\right]\delta b_r \delta b_s\right\} g(\mathbf{b}) d\mathbf{b} \tag{66}$$

and covariance

$$COV\left([\mathbb{C}(\mathbf{b})]_r, [\mathbb{C}(\mathbf{b})]_s\right) = \int_{-\infty}^{+\infty} \left\{[\mathbb{C}(\mathbf{b})]_r - E\left[\mathbb{C}(\mathbf{b})\right]\right\} \times \left\{[\mathbb{C}(\mathbf{b})]_s - E\left[\mathbb{C}(\mathbf{b})\right]\right\} g(\mathbf{b}) d\mathbf{b} \tag{67}$$

can be obtained straightforwardly by observing that

$$\int_{-\infty}^{+\infty} g(\mathbf{b}) d\mathbf{b} = 1, \qquad \int_{-\infty}^{+\infty} \delta\mathbf{b} g(\mathbf{b}) d\mathbf{b} = 0, \quad \text{and} \quad \int_{-\infty}^{+\infty} \delta\mathbf{b}_r \delta\mathbf{b}_s g(\mathbf{b}) d\mathbf{b} = COV(b_r, b_s). \tag{68}$$

The second-order approximation of the expected value for the reduced stiffness matrix is

$$E\left[\mathbb{C}(\mathbf{b})\right] = \left[\mathbb{C}(\bar{\mathbf{b}})\right] + \frac{1}{2}\sum_r^n \sum_s^n \left[H_{b_r b_s}\mathbb{C}(\bar{\mathbf{b}})\right] \cdot COV(b_r, b_s). \tag{69}$$

Obtaining the second-order approximation is more complicate for variance but the first-order approximation has sufficient accuracy, hence the first-order accurate approximation of covariance is provided as:

$$COV\left([\mathbb{C}(\mathbf{b})], [\mathbb{C}(\mathbf{b})]\right) \approx \sum_r^n \sum_s^n \left[D_{b_r}\mathbb{C}(\bar{\mathbf{b}})\right]\left[D_{b_s}\mathbb{C}(\bar{\mathbf{b}})\right] \cdot COV(b_r, b_s). \tag{70}$$

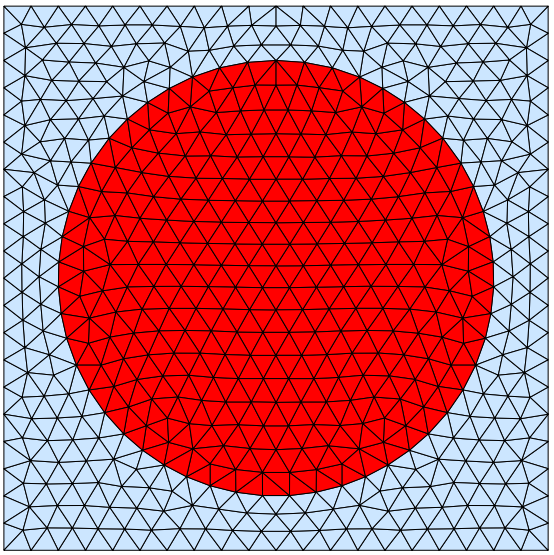

Fig. 2. Microstructure of the two-phase composite in Example 1.

6. Numerical examples

In this section, we detail three numerical examples to demonstrate the efficiency of the proposed approach in approximating the stochastic macroscopic constitutive behaviour for different material systems. In the first example a two phase composite is considered. The second example is also a two phase composite but includes a void. Both examples are considered plane strain. The third example investigates a fibre-reinforced composite lamina. Statistics of the homogenized elastic properties for these composites in terms of mean value and coefficient of variation are presented. Dependencies between the variations of input variables and statistics of the homogenized elastic properties are discussed for results obtained using the periodic boundary conditions as an example. The accuracy of the proposed method is verified by comparing the statistics of the homogenized elastic tensor against corresponding values obtained by using Monte Carlo simulation for linear, periodic, and traction boundary conditions, for the specific coefficient of variation (CV) with value of 0.1 of the constituent properties.

6.1. Example 1: two-phase composite

In this first example we study a two-phase composite comprising glass fibres and a resin matrix, with a fibre volume fraction that approximates to 50%. The material properties are assumed to be normally distributed random variables. The mean values of Poisson's ratios and Young's modulus for the matrix are $\nu_m = 0.34$ and $E_m = 4$ GPa, respectively, while the mean values of Young's modulus and Poisson's ratio for the fibres are $E_f = 84$ GPa and $\nu_f = 0.22$, respectively. The microstructure has been discretized into 1062 triangular elements with a total number of 572 nodes as shown in Fig. 2 by using DISTMESH2D [32].

Table 1 shows the means and coefficients of variation for the components $\bar{\mathbb{C}}_{11}$, $\bar{\mathbb{C}}_{12}$, and $\bar{\mathbb{C}}_{66}$ of the homogenized tensor obtained from Eqs. (69)–(70) using the developed PSMFE approach for three boundary conditions Eqs. (35), (46) and (60) with all four material properties having the same variation with a CV $= 0.1$. These are compared with the corresponding values obtained by coupling Monte Carlo simulation method (MCS) with the deterministic form of the homogenization method adopted in the present work, where the total number of random trials is taken as 5000. In general, the results in Table 1 indicate very good agreement at the level of the mean values, and sufficiently good agreement between the estimated values of coefficients of variation when comparing the proposed PSMFE and MCS for each of the three boundary conditions. Relatively, the results for $\bar{\mathbb{C}}_{12}$ show less agreement between these two approaches. Note that the variations in the values of the input material properties amplify to various degrees in the outputs. For instance, the variation in $\bar{\mathbb{C}}_{12}$ is about 0.3 compared to the input variation of 0.1; moreover, the variation in $\bar{\mathbb{C}}_{11}$ is larger than the variation of the input values and the variation in the $\bar{\mathbb{C}}_{66}$ is almost the same. In general, these amplifications result from the combination of Poisson's ratio and Young's modulus; the $\mathbf{C}_{11}$ and $\mathbf{C}_{12}$ terms in the

Table 1
Statistics of effective elastic property tensor for composite in Example 1.

B.C. model	Method	$\bar{\mathbb{C}}_{11}$		$\bar{\mathbb{C}}_{12}$		$\bar{\mathbb{C}}_{66}$	
		Mean	CV	Mean	CV	Mean	CV
Linear	MCS	15.48	0.1527	5.36	0.2887	4.28	0.0970
	PSMFE	15.42	0.1476	5.31	0.2739	4.28	0.0960
Periodic	MCS	15.11	0.1510	5.26	0.3064	3.12	0.0977
	PSMFE	15.05	0.1460	5.21	0.2904	3.12	0.0967
Traction	MCS	13.01	0.1566	6.84	0.2742	3.09	0.0969
	PSMFE	13.95	0.1507	6.79	0.2616	3.09	0.0969

Table 2
Comparison of estimates of effective engineering properties between PSMFE and Monte Carlo simulation.

EEP	Method	Mean value			Coefficient of variation		
		Displacement	Periodic	Traction	Displacement	Periodic	Traction
E	MCS	10.75	7.82	8.29	0.1069	0.0964	0.0950
	PSMFE	10.72	7.82	8.28	0.1019	0.0955	0.0942
ν	MCS	0.25	0.25	0.34	0.1006	0.1143	0.0807
	PSMFE	0.24	0.25	0.33	0.1050	0.1163	0.0828

Table 3
Comparison of computational time (seconds) between PSMFE and Monte Carlo simulation.

B.C. model	Method	Example 1	Example 2	Example 3
Linear	MCS	6555	47539	84992
	PSMFE	6.39	17.73	98.69
Periodic	MCS	8398	57789	102281
	PSMFE	9.97	24.78	135.21
Traction	MCS	11141	75195	121484
	PSMFE	17.23	30.14	157.48

stiffness matrix for plain strain state are $E_m(1-\nu_m)/(1+\nu_m)(1-2\nu_m)$ and $E_m\nu_m/(1+\nu_m)(1-2\nu_m)$, respectively, for the matrix, and $E_f(1-\nu_f)/(1+\nu_f)(1-2\nu_f)$ and $E_f\nu_f/(1+\nu_f)(1-2\nu_f)$, respectively, for the fibre. Comparing $\mathbf{C}_{11}$ with $\mathbf{C}_{12}$, the amplification decreases for $\bar{\mathbb{C}}_{11}$ to some extent due to the negative correlation between E and $-E\nu$.

Moreover, a comparison of the statistics of the effective engineering properties (EEP) obtained from the proposed PSMFE approach and the MCS method is given in Table 2. There is good agreement between PSMFE and MCS on mean values and coefficients of variation for the effective Young's modulus and Poisson ratio. In addition, to investigate the computational efficiency of the proposed method, computational times required by the PSMFE and MCS with 5000 samples for the same RVE are recorded. As shown in Table 3, the time using PSMFE is generally very short. It indicates that there are substantial reductions in the computational time using the present PSMFE instead of MCS.

To illustrate the relative importance of the random variables and quantitatively investigate the influence of the variations in constituent material properties on the coefficients of variation and mean values in the homogenized elasticity tensor, Fig. 3 shows how the coefficients of variation and mean values of $\bar{\mathbb{C}}_{11}$, $\bar{\mathbb{C}}_{12}$ and $\bar{\mathbb{C}}_{66}$ vary as a function of coefficient of variation in each material property of the constituents for the periodic boundary condition case. In these figures, the abscissa represents the coefficient of variation of input parameter, here the material properties, and the vertical axis represents the resultant coefficient of variation in the component of the effective elastic tensor. The graphs on the left in Fig. 3 illustrate the dependencies for the mean values, and the graphs on the right give those for the coefficients of variation. The study shows that the mean values marginally decrease with an increase in the coefficients of variations of Young's modulus and Poisson's ratio of the fibre, and Young's modulus of the matrix, but

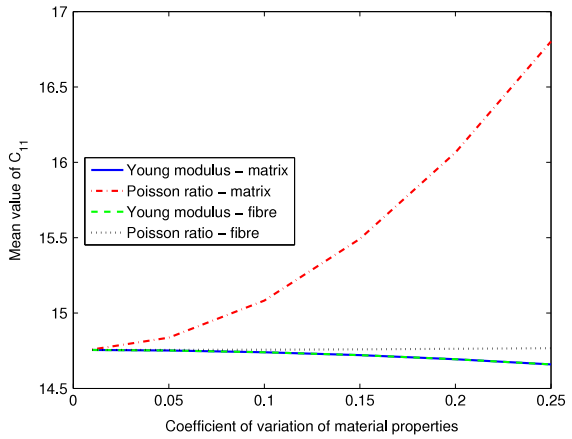

(a) Mean value of $\bar{\mathbb{C}}_{11}$.

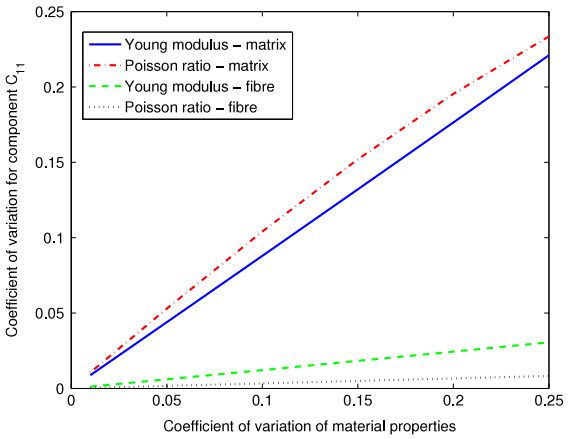

(b) Coefficent of variation of $\bar{\mathbb{C}}_{11}$.

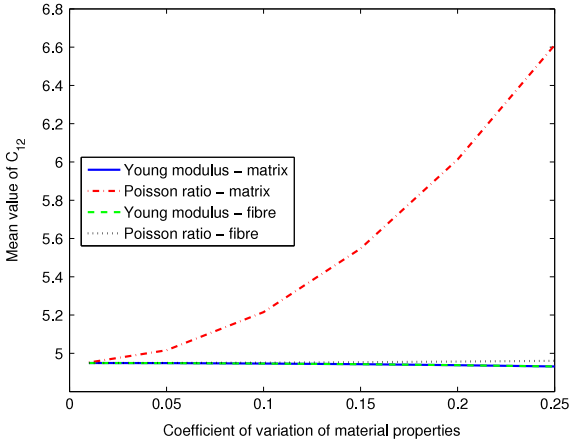

(c) Mean value of $\bar{\mathbb{C}}_{12}$.

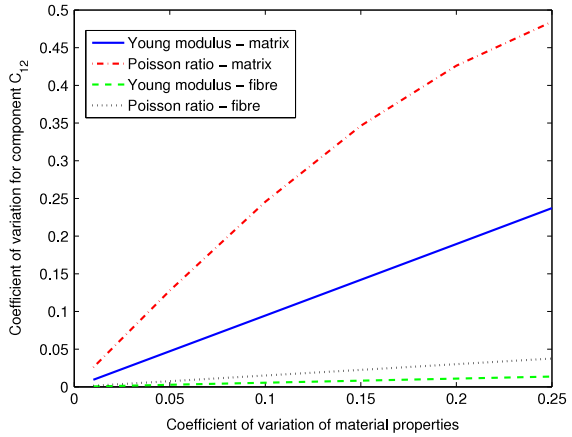

(d) Coefficient of variation of $\bar{\mathbb{C}}_{12}$.

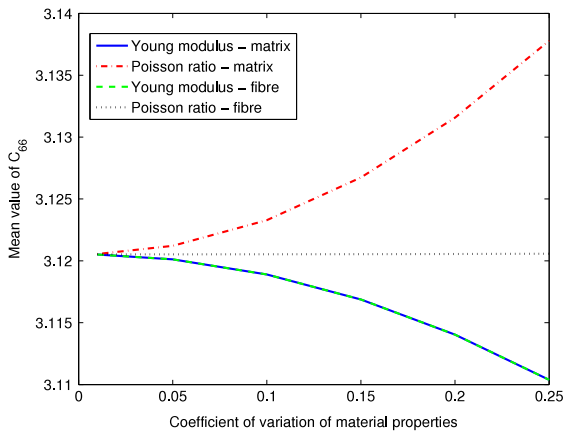

(e) Mean value of $\bar{\mathbb{C}}_{66}$.

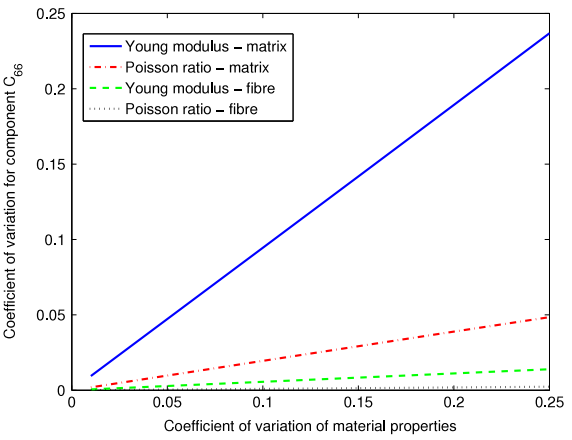

(f) Coefficient of variation of $\bar{\mathbb{C}}_{66}$.

Fig. 3. Mean value and coefficient of variation for different components of homogenized elasticity tensor with respect to coefficient of variation of material properties of the constituents in Example 1.

that the mean values increase with increasing coefficient of variation for Poisson's ratio of matrix. Positive correlation has been identified as the CVs for the components of the homogenized elastic tensor become larger with increasing

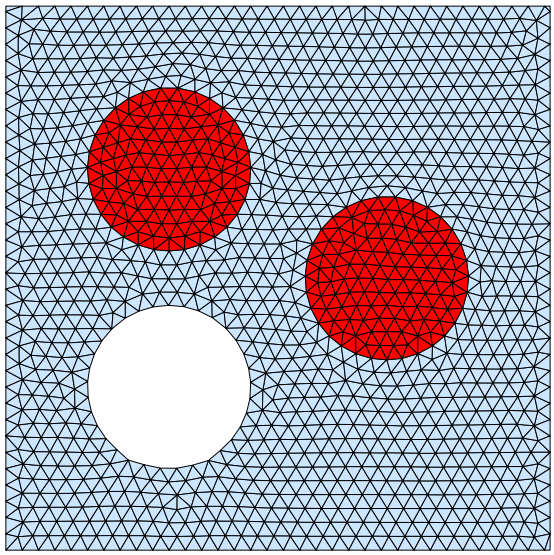

Fig. 4. Microstructure of the two-phase composite with hole in Example 2.

Table 4
Statistics of effective elastic property tensor for composite in Example 2.

B.C. model	Method	$\bar{\mathbb{C}}_{11}$		$\bar{\mathbb{C}}_{12}$		$\bar{\mathbb{C}}_{66}$	
		Mean	CV	Mean	CV	Mean	CV
Linear	MCS	30.40	0.1235	11.76	0.2191	9.25	0.0993
	PSMFE	30.40	0.1215	11.75	0.2128	9.25	0.0996
Periodic	MCS	29.01	0.1219	11.58	0.2121	8.50	0.0996
	PSMFE	28.98	0.1193	11.56	0.2057	8.49	0.0999
Traction	MCS	26.16	0.1218	11.59	0.1987	7.62	0.0990
	PSMFE	26.22	0.1199	11.59	0.1915	7.61	0.1000

variability of the constituent material properties. In general, the statistics of the components of the homogenized elastic tensor are most significantly influenced by variability in the properties of the matrix.

6.2. Example 2: two-phase composite with hole

Following Example 1, we investigate a two-phase composite that contains a void and two stiff inclusions embedded in a soft matrix, similar to that considered in [31] and shown in Fig. 4. The side length of the considered square RVE is $h = 1.0$, and the diameter of the hole and inclusions is $d = 0.3$. The hole is located at $(-0.2, -0.2)$, and the two inclusions are at $(-0.2, 0.2)$ and $(0.2, 0)$ in a coordinate system positioned at the centre of the cell. Hence, the fibre volume fraction is about 14%. Again, the constituents are assumed to be isotropic and linearly elastic, and the four material properties are considered as random variables with Normal distributions. Mean values of Poisson's ratios are $\nu_m = \nu_f = 0.30$, and mean values of Young's moduli are $E_m = 20.8264$ MPa and $E_f = 100E_m = 2082.64$ MPa for matrix and inclusion, respectively. The microstructure has been discretized into 2551 three-noded isoparametric triangle elements with a total number of 1360 nodes using DISTMESH2D [32] as shown in Fig. 4.

To investigate the accuracy of the PSMFE method, a comparison between the present PSMFE and MCS with 5000 samples for the expected values and coefficients of variation for the components $\bar{\mathbb{C}}_{11}$, $\bar{\mathbb{C}}_{12}$, and $\bar{\mathbb{C}}_{66}$ is performed for three boundary conditions (Eqs. (35), (46) and (60)). As with Example 1, all four independent material properties have coefficients of variation of CV = 0.1. The outcomes of these numerical studies are summarized in Table 4. Very good agreement between the proposed PSMFE and MCS is observed for values of mean and CV for various components of the homogenized elastic tensor with different boundary conditions. Similarly, the variations in inputs get amplified in $\bar{\mathbb{C}}_{11}$ and $\bar{\mathbb{C}}_{12}$ due to the combined effects of Poisson's ratio and Young's modulus.

Table 5
Material properties of graphite fibre and epoxy matrix for Example 3.

	Fibre	Matrix
Longitudinal Young's modulus, E_1, (GPa)	233	4.62
Transverse Young's modulus, E_2, (GPa)	23.1	4.62
Longitudinal Poisson's ratio, v_{12}	0.2	0.36
In-plane Shear modulus, G_{12}, (GPa)	8.96	1.7

Fig. 5 shows how the coefficient of variation and mean value for different components, $\bar{\mathbb{C}}_{11}$, $\bar{\mathbb{C}}_{12}$ and $\bar{\mathbb{C}}_{66}$, of the homogenized elasticity tensor under periodic boundary conditions (Eq. (46)) vary as a function of the coefficient of variation for each material property. In these figures, the abscissa represents the coefficient of variation of input parameter, here the material properties, and the vertical axis represents the resultant coefficient of variation in the component of the effective elastic tensor. The graphs on the left side of Fig. 5 illustrate the sensitivities of the mean values, and on the right, the sensitivities for the coefficients of variation. These results show the mean values increase with increasing coefficient of variation of Poisson's ratio of the matrix, whilst small negative correlations are observed for increases of coefficient variations of Young's modulus and Poisson's ratio of the fibre and Young's modulus of the matrix. From these observations, the variabilities of the properties of matrix play the most important role in determining the statistics of the components of the homogenized elastic tensor.

6.3. Example 3: fibre-reinforced composite lamina

A lamina made of fibres in a matrix is studied in this example in order to demonstrate applicability of the proposed methodology. The configuration is presented in Fig. 6(a). Due to the small thickness of a layer compared to the other two dimensions, the layer is considered as to be under plane stress condition [33]. The discretized RVE is shown in Fig. 6(b). The RVE contains a graphite-reinforced polymer composite with fibre volume fraction of 60%. The matrix is assumed to have elastic isotropic properties (Young's modulus and Poisson's ratio denoted by E_m and ν_m, respectively), while the graphite fibre is taken to be transversely isotropic, and to be defined by four independent constants, E_1^f, E_2^f, ν_{12}^f and G_{12}^f for longitudinal Young's modulus, transverse Young's modulus, and in-plane Poisson's ratio and shear modulus, respectively. These constants are consistent with plane-stress analysis. Hence, the homogenized constitutive model of the composite has six independent constants. The mean values of the material characteristics for the computational analysis are listed in Table 5 as indicated in [33]. Thus the variability of the homogenized elastic tensor due to variability of these six parameters of the constituent materials is quantified.

As with the previous two examples, to investigate the accuracy of the PSMFE method, the expected values and coefficients of variation for the components $\bar{\mathbb{C}}_{11}$, $\bar{\mathbb{C}}_{12}$, $\bar{\mathbb{C}}_{22}$ and $\bar{\mathbb{C}}_{66}$, calculated through (Eqs. (69)–(70)), are compared to the corresponding values obtained by Monte Carlo simulation method (MCS) where the total number of samples is taken as 5000. The six independent material properties are assumed to have coefficients of variation of 0.1. The results for all three types of boundary conditions (Eqs. (35), (46) and (60)) are listed in Table 6. In general, this shows a very good agreement between the present PSMFE and MCS for both the mean and CV for various components of the homogenized elastic tensor for the linear and periodic boundary conditions. It should be noted that for the traction boundary condition both the PSMFE and the MCS methodologies fail to obtain reasonable estimates for the homogenized elastic tensor. The inability of both approaches to achieve meaningful results demonstrates that this issue is not with the stochastic formulation, but rather with the homogenization methodology. Numerical studies have shown that it is probably caused by the fact that the matrix is soft compared with the fibres which, under traction boundary conditions, leads to deformation mainly of the matrix without deformation of the fibres. It is only when the stiffness of the matrix approaches that of the fibre that reasonable results are obtained from the traction boundary conditions. Conversely, the displacement and periodic boundary conditions deform both fibres and matrix so the effective stiffness comprises contributions from both the matrix and fibres, leading to reasonable predictions for the effective elastic tensor.

Comparison of the statistics of the effective engineering properties obtained from PSMFE and MCS was conducted to illustrate the feasibility of the proposed method. A unidirectional composite can be treated as a transversely isotropic material. Therefore, four effective engineering properties, E_1, E_2, ν_{12} and G_{12}, can be recovered from the plane stress case. Furthermore, the commonly used classic rule of mixture is also adopted here, and it is combined with Monte

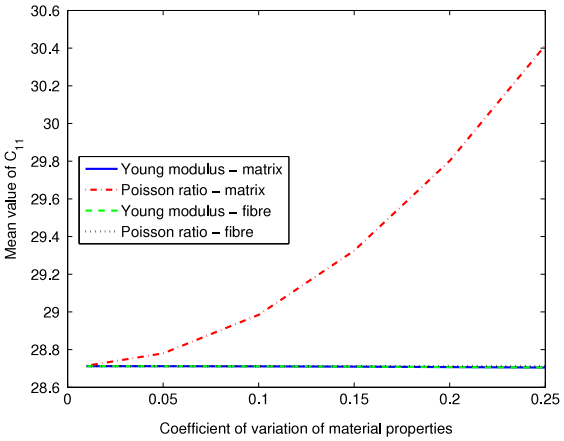

(a) Mean value of $\bar{\mathbb{C}}_{11}$.

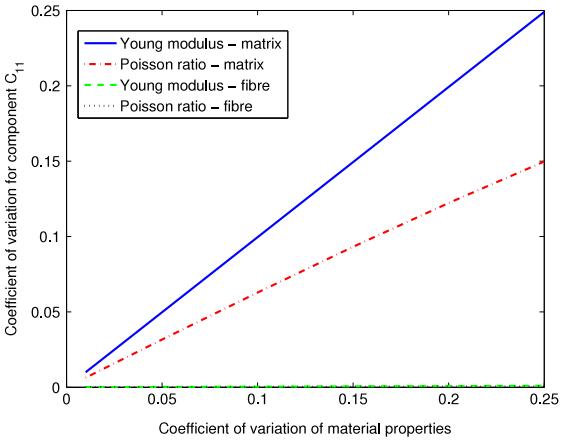

(b) Coefficient of variation of $\bar{\mathbb{C}}_{11}$.

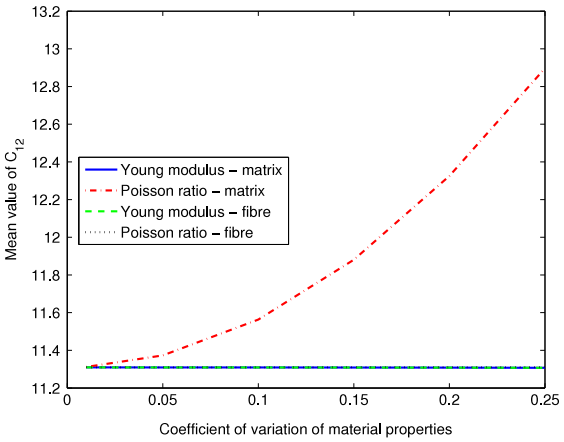

(c) Mean value of $\bar{\mathbb{C}}_{12}$.

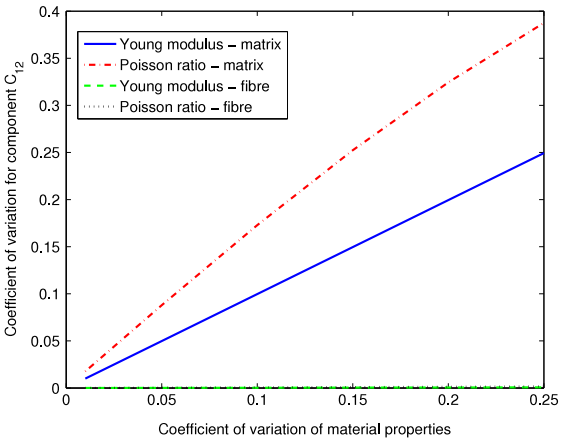

(d) Coefficient of variation of $\bar{\mathbb{C}}_{12}$.

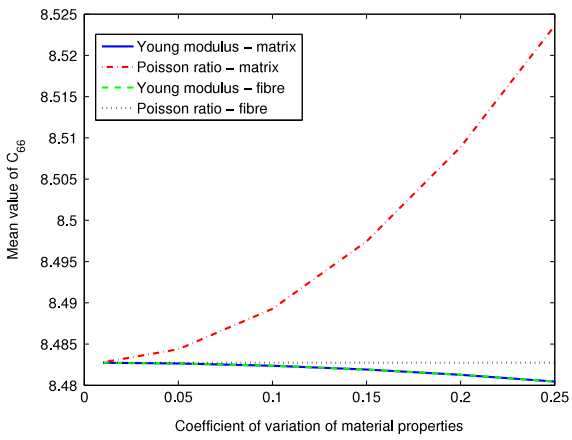

(e) Mean value of $\bar{\mathbb{C}}_{66}$.

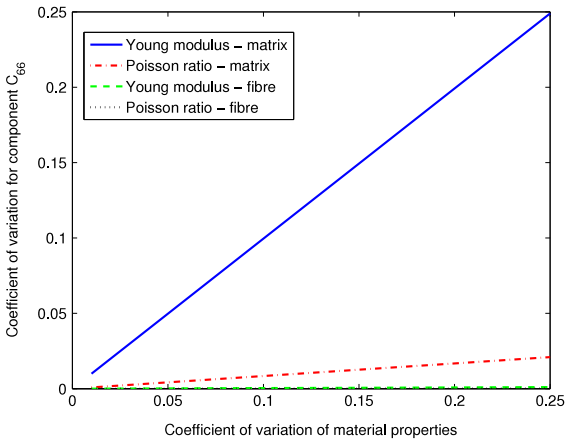

(f) Coefficient of variation of $\bar{\mathbb{C}}_{66}$.

Fig. 5. Mean value and coefficient of variation for different components of homogenized elasticity tensor with respect to coefficient of variation of material properties of the constituents in Example 2.

Table 6
Mean values and coefficients of variation for the effective elasticity tensor components for composite in Example 3.

B.C. model	Method	$\bar{\mathbb{C}}_{11}$		$\bar{\mathbb{C}}_{12}$		$\bar{\mathbb{C}}_{22}$		$\bar{\mathbb{C}}_{66}$	
		Mean	CV	Mean	CV	Mean	CV	Mean	CV
Linear	MCS	142.29	0.1004	2.77	0.1126	10.95	0.0726	5.48	0.0799
	PSMFE	142.37	0.0982	2.77	0.1106	10.96	0.0717	5.47	0.0793
Periodic	MCS	142.27	0.1004	2.61	0.1213	9.85	0.0830	3.29	0.0842
	PSMFE	142.34	0.0982	2.61	0.1193	9.86	0.0822	3.30	0.0840
Traction	MCS	23.21	0.0816	3.44	0.1428	9.85	0.0829	3.29	0.0842
	PSMFE	23.23	0.0812	3.43	0.1404	9.85	0.0821	3.30	0.0840

Table 7
Comparison of estimates of effective engineering properties between PSMFE and Monte Carlo simulation.

EEP	Method	Mean value			Coefficient of variation		
		Displacement	Periodic	Traction	Displacement	Periodic	Traction
E_1	MCS-Mix		141.74			0.0989	
	MCS	141.59	141.57	22.00	0.1009	0.1009	0.0821
	PSMFE	141.66	142.65	22.03	0.0987	0.0987	0.0817
E_2	MCS-Mix		8.84			0.0803	
	MCS	10.90	9.80	9.33	0.0721	0.0825	0.0806
	PSMFE	10.90	9.81	9.34	0.0710	0.0815	0.0799
ν_{12}	MCS-Mix		0.26			0.0704	
	MCS	0.25	0.26	0.35	0.0728	0.0718	0.0974
	PSMFE	0.25	0.26	0.35	0.0720	0.0710	0.0960
G_{12}	MCS-Mix		3.29			0.0837	
	MCS	5.48	3.29	3.29	0.0799	0.0842	0.0842
	PSMFE	5.47	3.30	3.30	0.0792	0.0838	0.0838

Carlo simulation method to consider randomness in constituent material properties. Results are listed in Table 7, where MCS-Mix represents results obtained by combining the classic rule of mixture with MCS. Note that the rule of mixture only provides one set of results as it does not consider different boundary conditions. For E_1, both the computational homogenization method and the rule of mixture provide similar results except for the traction boundary condition case of computational homogenization. For E_2, there are differences between the computational homogenization method and the rule of mixture. They may be caused by the widely accepted fact that the rule of mixture lacks the capability to consider the through thickness term. In general, the results reconfirm that the proposed PSMFE method can produce satisfactory results in comparison to those obtained by the MCS.

Fig. 7 shows how the coefficients of variation for different components of the homogenized elasticity tensor under periodic boundary conditions (Eq. (46)) vary as a function of the coefficient of variation for constituent material properties. In these figures, the horizontal axis represents the coefficient of variation of the input, and the vertical axis represents the resultant coefficient of variation in the component of the effective elastic tensor. To avoid displaying unnecessarily large volume of data, only those characteristics that have significant influence (e.g. greater than approximately 10%) on the coefficient of variation for the components of the homogenized elastic tensor are shown.

The variation of $\bar{\mathbb{C}}_{11}$ is seen to be significantly dependent on the modulus of the fibre compared with other parameters; the variation of $\bar{\mathbb{C}}_{12}$ is strongly correlated to Young's modulus and Poisson's ratio of the matrix and the transverse Young's modulus and Poisson's ratio of the fibre; the variation of $\bar{\mathbb{C}}_{22}$ depends on Young's modulus and Poisson's ratio of the matrix and the transverse Young's modulus of the fibre; the Young's modulus of the matrix has a substantial influence on the variation of $\bar{\mathbb{C}}_{66}$ with Poisson's ratio of the matrix and the shear modulus of the fibre also making important contributions.

The relation of the variation of selected "important" input variables to the mean values of different components of the homogenized elasticity tensor is illustrated in Fig. 8. It has been observed that: the mean value of $\bar{\mathbb{C}}_{11}$ increases with increasing variability of the longitudinal Young's modulus of the fibres; the mean values of $\bar{\mathbb{C}}_{12}$, $\bar{\mathbb{C}}_{22}$ and $\bar{\mathbb{C}}_{66}$

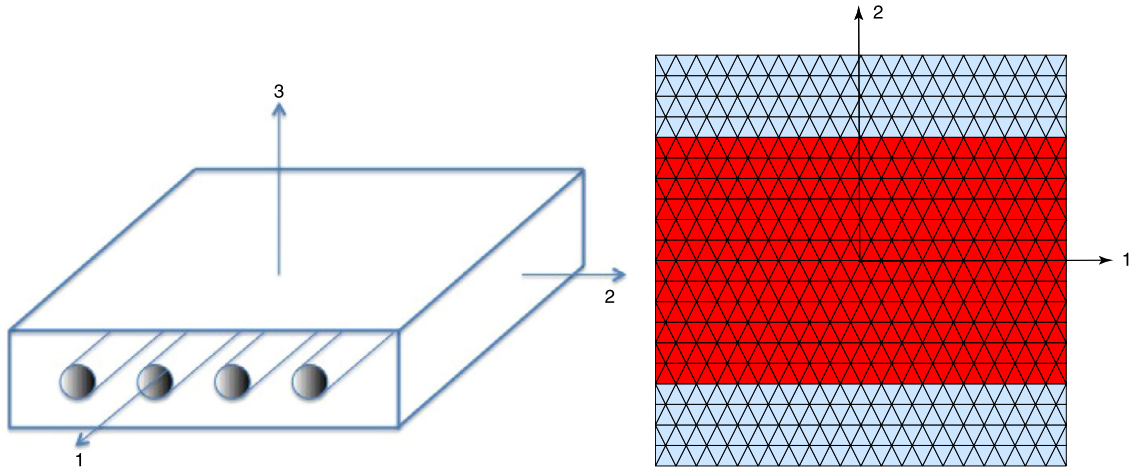

(a) Coordinate system and profile.

(b) Discretization of RVE.

Fig. 6. Fibre-reinforced lamina in Example 3.

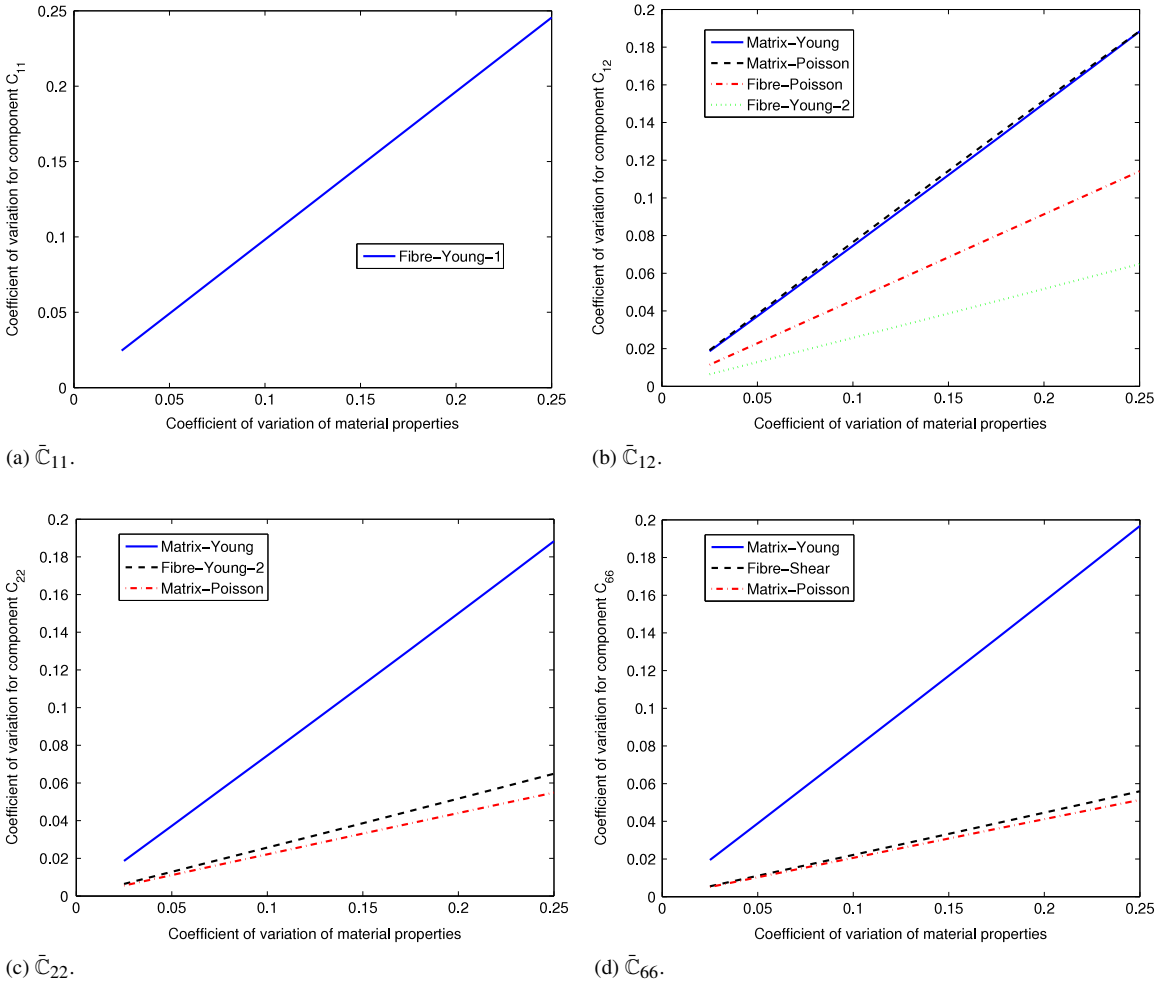

(a) $\bar{\mathbb{C}}_{11}$.

(b) $\bar{\mathbb{C}}_{12}$.

(c) $\bar{\mathbb{C}}_{22}$.

(d) $\bar{\mathbb{C}}_{66}$.

Fig. 7. Coefficient of variation for different components of homogenized elasticity tensor with respect to coefficient of variation of material properties of the constituents in Example 3.

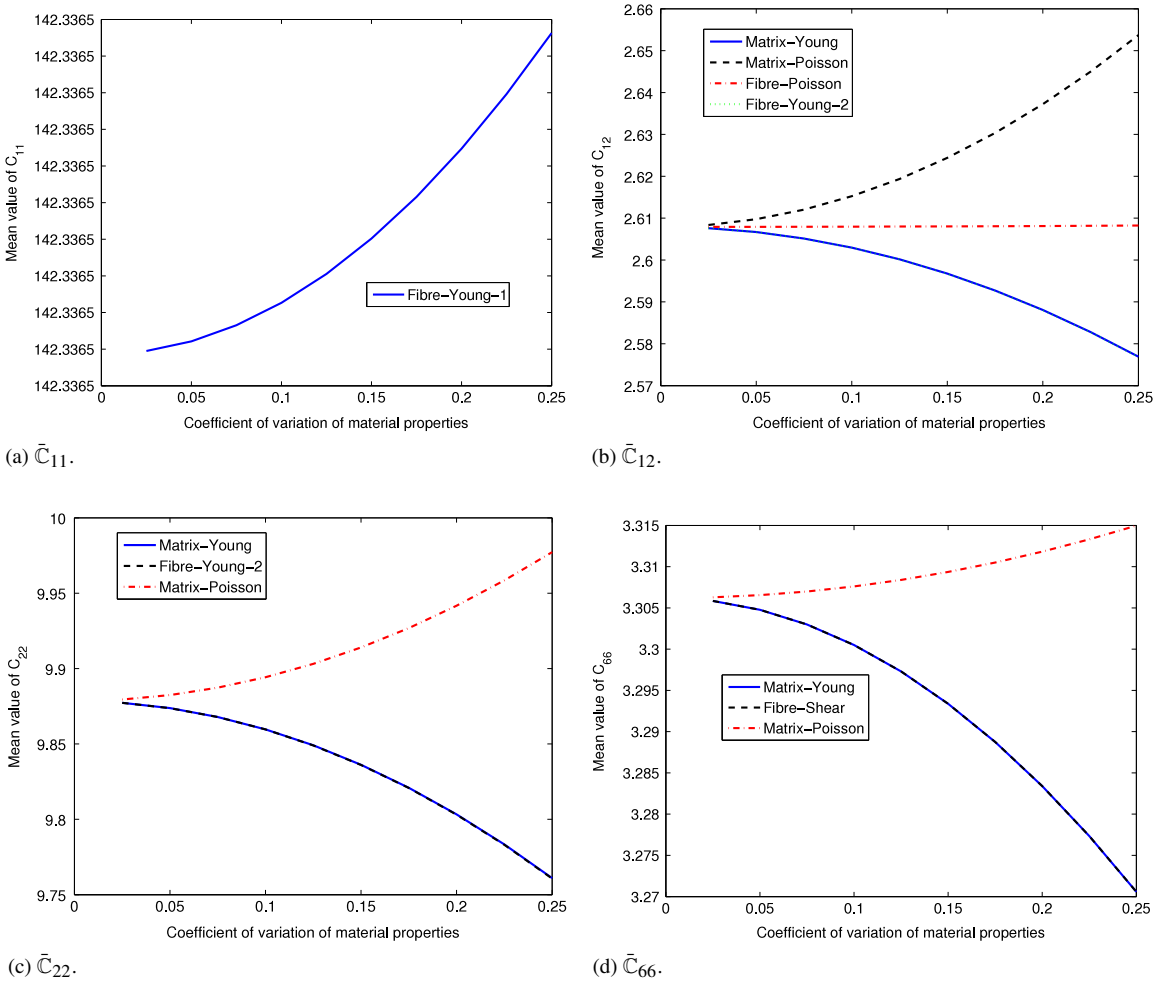

(a) $\bar{\mathbb{C}}_{11}$. (b) $\bar{\mathbb{C}}_{12}$.

(c) $\bar{\mathbb{C}}_{22}$. (d) $\bar{\mathbb{C}}_{66}$.

Fig. 8. Mean value for different components of homogenized elasticity tensor with respect to coefficient of variation of material properties of the constituents in Example 3.

increase with increasing variability of Poisson's ratio of the matrix, whilst decreasing with CV of the matrix Young's modulus.

7. Conclusions

In this paper, a stochastic multi-scale finite element method is proposed for the homogenization analysis of composite materials when randomness in the material constituent properties is taken into consideration. In the proposed method, the computational homogenization scheme proposed in [29,5], which introduces a hierarchy of boundary conditions at the microscale and allows for direct treatment of micro-to-macro transitions, is adopted to estimate the overall elasticity property. The second-order perturbation technique is used to approximate the uncertainty in the stiffness matrix of microstruture arising from the randomness of microscopic material properties.

Three numerical examples have been provided to demonstrate the capability of the proposed method in capturing variability in effective elastic properties for composites induced by randomness of constituent material properties. Statistics in terms of mean and coefficient of variation of the effective elastic properties for these three examples are obtained by the proposed perturbation-based stochastic multi-scale homogenization approach and compared with the results obtained using Monte Carlo simulation. The comparisons demonstrate that the proposed method provides sufficiently accurate estimates of the mean value and coefficient of variation of the effective elastic properties. Furthermore, the use of the proposed method to investigate the relation of statistics of the overall elasticity

characteristics with the randomness of the constituent material properties has been demonstrated, and the significance of the material properties identified for three types of composite materials.

Acknowledgements

The authors gratefully acknowledge the financial support provided for this study by the UK Engineering and Physical Sciences Research Council (EPSRC) under grant reference EP/K026925/1. The authors are also grateful to Professor Eduardo de Souza Neto of the Zienkiewicz Centre for Computational Engineering at Swansea University, UK, for his computational homogenization Matlab code, Microcell, which formed the basis for this stochastic multiscale FE method.

References

[1] W.E.B. Engquist, X. Li, W. Ren, E. Vanden-Eijnden, Heterogeneous multiscale methods: A review, Commun. Comput. Phys. 2 (3) (2007) 367–450.
[2] P. Kanouté, D.P. Boso, J.L. Chaboche, B.A. Schrefler, Multiscale methods for composites: A review, Arch. Comput. Methods Eng. 16 (1) (2009) 31–75.
[3] T.I. Zohdi, Homogenization Methods and Multiscale Modeling, John Wiley & Sons, Ltd., 2004, pp. 407–430. Book section 12.
[4] M.G.D. Geers, V.G. Kouznetsova, W.A.M. Brekelmans, Multi-scale computational homogenization: Trends and challenges, J. Comput. Appl. Math. 234 (7) (2010) 2175–2182.
[5] D. Perić, E.A. de Souza Neto, R.A. Feijóo, M. Partovi, A.J.C. Molina, On micro-to-macro transitions for multi-scale analysis of non-linear heterogeneous materials: unified variational basis and finite element implementation, Internat. J. Numer. Methods Engrg. 87 (1–5) (2011) 149–170.
[6] M.A. Gutiérrez, R. De Borst, Numerical analysis of localization using a viscoplastic regularization: influence of stochastic material defects, Internat. J. Numer. Methods Engrg. 44 (12) (1999) 1823–1841.
[7] M. Kamiński, Sensitivity studies for the effective characteristics of periodic multicomponent composites, Internat. J. Engrg. Sci. 44 (11–12) (2006) 757–777.
[8] S. Sriramula, M.K. Chryssanthopoulos, Quantification of uncertainty modelling in stochastic analysis of frp composites, Composites A 40 (11) (2009) 1673–1684.
[9] D.J. Lekou, T.P. Philippidis, Mechanical property variability in frp laminates and its effect on failure prediction, Composites B 39 (7–8) (2008) 1247–1256.
[10] L. Huyse, M. Maes, Random field modeling of elastic properties using homogenization, J. Eng. Mech. 127 (1) (2001) 27–36.
[11] J. Hohe, C. Beckmann, Probabilistic homogenization of hexagonal honeycombs with perturbed microstructure, Mech. Mater. 49 (0) (2012) 13–29.
[12] M. Kamiński, M. Kleiber, Stochastic structural interface defects in fiber composites, Int. J. Solids Struct. 33 (20) (1996) 3035–3056.
[13] S. Sakata, F. Ashida, T. Kojima, M. Zako, Three-dimensional stochastic analysis using a perturbation-based homogenization method for elastic properties of composite material considering microscopic uncertainty, Int. J. Solids Struct. 45 (3–4) (2008) 894–907.
[14] G. Stefanou, The stochastic finite element method: Past, present and future, Comput. Methods Appl. Mech. Engrg. 198 (9–12) (2009) 1031–1051.
[15] B. Hiriyur, H. Waisman, G. Deodatis, Uncertainty quantification in homogenization of heterogeneous microstructures modeled by xfem, Internat. J. Numer. Methods Engrg. 88 (3) (2011) 257–278.
[16] H. Dehmous, H. Welemane, Multi-scale reliability analysis of composite structures — application to the laroin footbridge, Eng. Failure Anal. 18 (3) (2011) 988–998.
[17] P. Sasikumar, R. Suresh, S. Gupta, Stochastic finite element analysis of layered composite beams with spatially varying non-gaussian inhomogeneities, Acta Mechanica (2013) 1–20.
[18] P.D. Spanos, A. Kontsos, A multiscale monte carlo finite element method for determining mechanical properties of polymer nanocomposites, Probab. Eng. Mech. 23 (4) (2008) 456–470.
[19] K. Terada, M. Hori, T. Kyoya, N. Kikuchi, Simulation of the multi-scale convergence in computational homogenization approaches, Int. J. Solids Struct. 37 (16) (2000) 2285–2311.
[20] D. Savvas, G. Stefanou, M. Papadrakakis, G. Deodatis, Homogenization of random heterogeneous media with inclusions of arbitrary shape modeled by xfem, Comput. Mech. 54 (5) (2014) 1221–1235.
[21] M. Kleiber, T.D. Hien, The Stochastic Finite Element Method - Basic Perturbation Technique and Computer Implementation, John Wiley & Sons, 1992.
[22] M. Kamiński, The Stochastic Perturbation Method for Computational Mechanics, John Wiley & Sons, 2013.
[23] M. Kamiński, M. Kleiber, Perturbation based stochastic finite element method for homogenization of two-phase elastic composites, Comput. Struct. 78 (6) (2000) 811–826.
[24] X.F. Xu, A multiscale stochastic finite element method on elliptic problems involving uncertainties, Comput. Methods Appl. Mech. Engrg. 196 (25–28) (2007) 2723–2736.
[25] L. Shen, X.F. Xu, Multiscale stochastic finite element modeling of random elastic heterogeneous materials, Comput. Mech. 45 (6) (2010) 607–621.
[26] M. Tootkaboni, L. Graham-Brady, A multi-scale spectral stochastic method for homogenization of multi-phase periodic composites with random material properties, Internat. J. Numer. Methods Engrg. 83 (1) (2010) 59–90.

[27] A. Clément, C. Soize, J. Yvonnet, Computational nonlinear stochastic homogenization using a nonconcurrent multiscale approach for hyperelastic heterogeneous microstructures analysis, Internat. J. Numer. Methods Engrg. 91 (8) (2012) 799–824.
[28] A. Clément, C. Soize, J. Yvonnet, Uncertainty quantification in computational stochastic multiscale analysis of nonlinear elastic materials, Comput. Methods Appl. Mech. Engrg. 254 (0) (2013) 61–82.
[29] D. Perić, E.A.d. de Souza Neto, A.J. CarneiroMolina, M. Partovi, On multiscale analysis of heterogeneous composite materials: implementation of micro-to-macro transitions in the finite element setting, in: Computational Methods in Applied Sciences, vol. 7, Springer Netherlands, 2007, pp. 165–185. Book section 10.
[30] V. Kouznetsova, W.A.M. Brekelmans, F.P.T. Baaijens, An approach to micro-macro modeling of heterogeneous materials, Comput. Mech. 27 (1) (2001) 37–48.
[31] C. Miehe, A. Koch, Computational micro-to-macro transitions of discretized microstructures undergoing small strains, Arch. Appl. Mech. 72 (4–5) (2002) 300–317.
[32] P. Persson, G. Strang, A simple mesh generator in matlab, SIAM Rev. 46 (2) (2004) 329–345.
[33] M.W. Hyer, Stree analysis of fiber-reinforced composite materials, in: Mechanical Engineering Series, McGraw-Hill, Boston, 1998.